Omnipose: a high-precision morphology-independent solution for bacterial cell segmentation

Kevin J. Cutler[1], Carsen Stringer[2], Paul A. Wiggins[1,3,*] and Joseph D. Mougous[4,5,*]

[1]Department of Physics, University of Washington, Seattle, WA 98195, USA

[2]HHMI Janelia Research Campus, Ashburn, VA, USA

[3]Department of Bioengineering, University of Washington, Seattle, WA 98195, USA

[4]Department of Microbiology, University of Washington, Seattle, WA 98109, USA

[5]Howard Hughes Medical Institute, University of Washington, Seattle, WA 98195, USA

* To whom correspondence should be addressed:

Email – pwiggins@uw.edu, mougous@uw.edu

1

1   **Abstract**

2   Advances in microscopy hold great promise for allowing quantitative and precise

3   readouts of morphological and molecular phenomena at the single cell level in bacteria.

4   However, the potential of this approach is ultimately limited by the availability of

5   methods to perform unbiased cell segmentation, defined as the ability to faithfully

6   identify cells independent of their morphology or optical characteristics. In this study, we

7   present a new algorithm, Omnipose, which accurately segments samples that present

8   significant challenges to current algorithms, including mixed bacterial cultures,

9   antibiotic-treated cells, and cells of extended or branched morphology. We show that

10   Omnipose achieves generality and performance beyond leading algorithms and its

11   predecessor, Cellpose, by virtue of unique neural network outputs such as the gradient of

12   the distance field. Finally, we demonstrate the utility of Omnipose in the characterization

13   of extreme morphological phenotypes that arise during interbacterial antagonism and on

14   the segmentation of non-bacterial objects. Our results distinguish Omnipose as a uniquely

15   powerful tool for answering diverse questions in bacterial cell biology.

Introduction

16

17   Although light microscopy is a valuable tool for characterizing cellular and sub-

18   cellular structures and dynamics, quantitative analysis of microscopic data remains a

19   persistent challenge[1]. This is especially pertinent to the study of bacteria, many of which

20   have dimensions in the range of optical wavelengths. Thus, their cell body is composed

21   of a small number of pixels (*e.g.,* ~100-300 px^2 for *E. coli* at 100x magnification). At this

22   scale, accurate subcellular localization requires defining the cell boundary with single-

23   pixel precision. The process of defining cell boundaries within micrographs is termed cell

24   segmentation and this is a critical first step in current image analysis pipelines[2,3].

25   In addition to their small size, bacteria adopt a wide range of morphologies.

26   Although many commonly studied bacteria are well-approximated by idealized rods or

27   spheres, there is growing interest in bacteria with more elaborate shapes[4]. Some examples

28   include Streptomycetales, which form long filamentous and branched hyphal structures[5],

29   and Caulobacterales, which generate extended appendages distinct from their cytoplasm[6].

30   Furthermore, microfluidic devices are allowing researchers to capture the responses of

31   bacteria to assorted treatments such as antibiotics, which often result in highly irregular

32   morphologies[7]. Whether native or induced, atypical cell morphologies present a distinct

33   problem at the cell segmentation phase of image analysis[8,9]. This is compounded when

34   such cells are present with those adopting other morphologies, as is the case in many

35   natural samples of interest[10]. To date, there are no solutions for segmenting bacterial cells

36   of assorted shape and size in a generalizable manner[1].

37   Cell segmentation is a complex problem that extends beyond microbiological

38   research, thus many solutions are currently available in image analysis programs[8,9,11-27].

3

39   Most of these solutions use traditional image processing techniques such as the

40   application of an intensity threshold to segment isolated cells; however, this approach

41   does not perform well for cells in close contact and it requires extensive parameter-tuning

42   in order to optimize for a given cell type. SuperSegger was developed to address these

43   issues specifically in bacterial phase contrast images[13]. This program utilizes both

44   traditional image filtering techniques and a shallow neural network to correct for errors

45   that thresholding and watershed segmentation tend to produce.

46   Deep neural networks (DNNs) are now widely recognized as superior tools for

47   cell segmentation[28]. Unlike traditional image processing, machine-learning approaches

48   such as DNNs require training on a ground-truth dataset of cells and corresponding

49   labels. Trained DNNs are thus limited in applicability to images that are representative of

50   those in the training dataset. Early DNN approaches were based on the Mask R-CNN

51   architecture[24], whereas more recent algorithms such as StarDist, Cellpose, and MiSiC are

52   based on the U-Net architecture[12,15,26]. Pachitariu and colleagues showed that Cellpose

53   outperforms Mask R-CNN and StarDist on a variety of cell types and cell-like objects,

54   distinguishing it as a general solution for cell segmentation[12]. Notably, the representation

55   of bacteria in their study was limited. MiSiC was developed as a general DNN-based

56   solution for bacterial segmentation; however, the authors of MiSiC did not provide

57   comparisons to other DNN algorithms[15]. Here, we evaluated the performance of state-of-

58   the-art cell segmentation algorithms on a diverse collection of bacterial cells. Our

59   findings motivated the design of a new algorithm, Omnipose, that significantly

60   outperforms all previous cell segmentation algorithms across a wide range of bacterial

61   cell sizes, morphologies, and optical characteristics. We have made Omnipose and all

62   associated data immediately available to researchers, and we anticipate that our model –

63   without retraining – can be applied to diverse bacteriological systems. Furthermore,

64   following the incorporation of additional ground truth data, Omnipose could serve as a

65   platform for segmenting various eukaryotic cells and extended, anisotropic objects more

66   broadly.

67

68   **Results**

69   **Evaluation of bacterial cell segmentation algorithms**

70   Numerous image segmentation algorithms have been developed, and the

71   performance of many of these on bacterial cells is documented[1]. These broadly fall into

72   three categories: (*i*) traditional image processing approaches (*e.g.,* thresholding,

73   watershed), (*ii*) traditional/machine learning hybrid approaches, and (*iii*) deep neural

74   network (DNN) approaches. Given the goal of developing software with the capacity to

75   recognize bacteria universally, we sought to identify strongly performing algorithms for

76   further development. An unbiased, quantitative comparison of cell segmentation

77   algorithms on bacterial cells has not been performed; thus, we selected one or more

78   representatives from each category for our analysis: Morphometrics[23] (*i*), SuperSegger[13]

79   (*ii*), Mask R-CNN[27], StarDist[26], MiSiC[15], and Cellpose[12] (*iii*). For a detailed review of

80   these choices, see Methods.

81   For training and benchmarking these algorithms, we acquired micrographs of

82   assorted bacterial species representing diverse morphologies and optical characteristics.

83   Many studies of bacteria involve mutations or treatments that cause extreme

84   morphologies. To capture this additional diversity, we included wild-type and mutant

5

85   bacteria grown in the presence of two beta-lactam antibiotics, cephalexin and aztreonam,

86   and A22, which targets MreB[29]. Finally, based on our interest in microbial communities,

87   we acquired images of mixtures of bacteria which display distinct morphologies and

88   optical characteristics. In total, we collected 4833 images constituting approximately

89   700,900 individual cells deriving from 14 species (Extended Data Table 1). Next, we

90   developed a streamlined approach for manual cell annotation and applied it to these

91   images (see Methods), yielding 46,000 representative annotated cells that serve as our

92   ground-truth dataset. We arbitrarily split this data into a 27,000-cell training set and a

93   19,000-cell benchmarking set. Relevant cellular metrics did not differ substantially

94   between the groups, confirming that the benchmarking set faithfully represents the

95   training set (Extended Data Fig. 1).

96   To facilitate direct comparison of the algorithms, we first optimized their

97   performance against our data. For the DNN approaches, each algorithm was trained on

98   our dataset using developer-recommended parameters. Morphometrics and SuperSegger

99   cannot be automatically optimized using ground-truth data; therefore, we manually

100   identified settings that optimized the performance of these algorithms against our dataset

101   (see Methods). As a quantitative measure for algorithm performance, we compared their

102   average Jaccard Index (JI) as a function of intersection over union (IoU) threshold – a

103   well-documented approach for evaluating image segmentation (Fig. 1a)[30,31]. IoU values

104   lie between zero and one, with values greater than 0.8 marking the point at which masks

105   become indistinguishable from ground truth by the expert human eye (Extended Data

106   Fig. 2)[30]. This analysis showed that DNN-based approaches significantly outperform

107   other algorithms. However, within the DNN group, substantial differences in

108   performance were observed; Cellpose and StarDist outperform Mask R-CNN and MiSiC

109   at high IoU thresholds. The performance of all algorithms varied greatly across the

110   images in our ground-truth dataset, with much of this variability delineated by cell type

111   and morphology categories (Fig. 1b-g). Whereas all other algorithms exhibited visible

112   segmentation errors in two of the three cell categories we defined, errors by Cellpose –

113   the best overall performing algorithm at high IoU thresholds – were only apparent in

114   elongated cells (Fig. 1h-j).

115

116   **Motivation for a new DNN-based segmentation algorithm**

117   Our comparison revealed that Cellpose offers superior performance relative to the

118   other segmentation algorithms we analyzed, and for this reason, we selected this

119   algorithm for further development. Notably, even at the high performance levels of

120   Cellpose, only 83% of predictions on our benchmarking dataset are above 0.8 IoU. This

121   limits the feasibility of highly quantitative studies such as those involving subcellular

122   protein localization or cell–cell interactions.

123   Cellpose utilizes a neural network that is trained on ground-truth examples to

124   transform an input image into several intermediate outputs, including a scalar probability

125   field for identifying cell pixels (Extended Data Fig. 3a, panels *i-iii*)[12]. Cellpose is unique

126   among DNN algorithms by the addition of a vector field output, which is defined by the

127   normalized gradient of a heat distribution from the median cell pixel coordinate

128   (Extended Data Fig. 3a, panels *iv,v*). This vector field directs pixels toward a global cell

129   center via Euler integration, allowing cells to be segmented based on the points at which

130   pixels coalesce (Extended Data Fig. 3b). In contrast to other algorithms, this approach for

7

131   reconstructing cells is size- and morphology-independent, insofar as the cell center can be

132   correctly defined.

133   To further interrogate the accuracy of Cellpose on our dataset, we evaluated its

134   performance as a function of cell size. We compared cell area against the number of

135   segmentation errors, calculated as the number of redundant or missing masks

136   corresponding to each ground-truth cell mask. This revealed a strong correlation between

137   cell size and segmentation errors, with the top quartile of cells accounting for 83% of all

138   errors (Fig. 2a). To understand the source of these errors, we inspected the flow field

139   output of many poorly segmented cells across a variety of species and growth conditions.

140   This showed that elongated cells, an important morphology often seen in both wild-type

141   and mutant bacterial populations, are particularly susceptible to over-segmentation (Fig.

142   2b). We attribute this to the multiple sinks apparent in the corresponding flow fields. In

143   the Cellpose mask reconstruction algorithm, pixels belonging to these cells are guided

144   into multiple centers per cell, fragmenting the cell into many separate masks.

145   We hypothesized that the observed defect in Cellpose flow field output is a

146   consequence of two distinct flow field types arising from our training dataset: those

147   where the median pixel coordinate, or 'center', lies within the cell (97.8%) and those

148   where it lies outside the cell (2.2%). In the latter, Cellpose projects the center point to the

149   nearest boundary pixel, ultimately leading to points of negative divergence on the cell

150   periphery that are chaotically distributed (Fig. 2c-e). On the contrary, non-projected

151   centers maintain a uniform field magnitude along the entire boundary and adhere to the

152   global symmetries of the cell (Extended Data Fig. 4a,d). A similar issue is also

153   encountered in cells with centers that are not projected but lie close to the boundary

8

154   (Extended Data Fig. 4b-d). Cells with a center point closer than 0.3 times the mean cell

155   diameter (a factor of 0.2 off-center) to the boundary account for an additional 8.5% of our

156   data. Neural networks can be exquisitely sensitive to the outliers in their training data[32];

157   therefore, we suspect that this small fraction of corrupt flow fields has significantly

158   impacted the performance of Cellpose.

159

160   **Development of a new DNN-based segmentation algorithm**

161   As there exists no straightforward means of defining a cell center for irregular

162   objects, we sought to develop a segmentation algorithm that operates independently of

163   cell center identification. We built our new algorithm, which we named Omnipose,

164   around the scalar potential known as the distance field (or distance transform), which

165   describes the distance at any point $\vec{x}$ in a bounded region Ω to the closest point on the

166   boundary $\partial\Omega$. Notably, this widely utilized construct is one of the intermediate outputs of

167   StarDist[32]. Whereas in StarDist it is used to seed and assemble star-convex polygons, its

168   use in Omnipose is to define a new flow field within the Cellpose framework. The use of

169   a distance field has several advantages. First, the distance field is defined by the eikonal

170   equation $\left|\vec{\nabla}\Phi(\vec{x})\right| = 1$, and so its gradient has unit magnitude throughout the bounded

171   region for which it is calculated. This grants it faster convergence and better numerical

172   stability when compared to alternative solutions producing similar fields (*e.g.,* screened

173   Poisson; see Methods) (Extended Data Fig. 5a). Second, the distance field is independent

174   of morphology and topology, meaning that it is applicable to all cells. Lastly, the

175   resulting flow field points uniformly from cell boundaries toward the local cell center,

176   coinciding with the medial axis, or skeleton, that is defined by the stationary points of the

9

177   distance field (Extended Data Fig. 5b). This critical feature allows pixels to remain

178   spatially clustered after Euler integration, solving the problem of over-segmentation seen

179   in Cellpose.

180   One challenge to using the distance field as the basis to our approach is that

181   traditional distance field algorithms like FMM (Fast Marching Method) are sensitive to

182   boundary pixilation[33], causing artifacts in the flow field that extend deep into the cell.

183   These artifacts are sensitive to pixel-scale changes at the cell perimeter, which we

184   reasoned would interfere with the training process. To solve this, we developed an

185   alternative approach based on FIM (Fast Iterative Method) that produces smooth distance

186   fields for arbitrary cell shapes and sizes (Fig. 3a, and see Methods)[34]. The corresponding

187   flow field is relatively insensitive to boundary features at points removed from the cell

188   boundary, a critical property for robust and generalized prediction by the Cellpose

189   network.

190   The use of the distance field additionally required a unique solution for mask

191   reconstruction. Whereas the pixels in a center-seeking field converge on a point, standard

192   Euler integration under our distance-derived field tends to cluster pixels into multiple thin

193   fragments along the skeleton, causing over-segmentation (Fig. 3b). We solved this with a

194   suppression factor of $(t + 1)^{-1}$ in each time step of the Euler integration. This reduces

195   the movement of each pixel after the first step $t = 0$, facilitating initial cell separation

196   while preventing pixels from clustering into a fragmented skeleton formation. The wider

197   distribution resulting from our suppression factor allows pixels to remain connected,

198   thereby generating a single mask for each cell in conjunction with a standard automated

199   pixel clustering algorithm (*e.g.,* DBSCAN)[35].

200

Omnipose demonstrates unprecedented segmentation accuracy of bacterial cells

201

202   With solutions to the major challenges of cell center-independent segmentation

203 incorporated into Omnipose, we proceeded to benchmark its performance. Remarkably,

204 across the IoU threshold range 0.5-1.0, Omnipose averages a JI >10-fold above that of

205 Cellpose (Fig. 4a). The difference in performance between the algorithms is particularly

206 pronounced within the high IoU range (0.75-1.0), where we observe an average of 170-

207 fold higher JI for Omnipose. At the 0.5-5 μm scale and with a typical microscope

208 configuration, quantitative measurements rely upon IoU values in this range, thus

209 Omnipose is uniquely suited for the microscopic analysis of bacterial cells.

210   To dissect the contributions of the individual Omnipose innovations to the overall

211 performance of the algorithm, we isolated the mask reconstruction component of

212 Omnipose and applied it to the Cellpose network output. This augmentation of Cellpose

213 modestly improved its performance to a roughly equivalent extent across all IoU

214 thresholds (Fig. 4a). Based on this, we attribute the remaining gains in performance by

215 Omnipose to its unique network outputs and our improvements to the Cellpose training

216 framework (see Methods).

217   Our analyses illuminated critical flaws in prior DNN-based approaches for the

218 segmentation of elongated cells, effectively preventing these algorithms from

219 generalizable application to bacteria (Fig. 1). To determine whether Omnipose overcomes

220 this limitation, we evaluated its performance as a function of cell area. Cell area serves as

221 a convenient proxy for cell length in our dataset, which is composed of both branched

222 and unbranched elongated cells. Whereas the Cellpose cell error rate remains above 9%

223   and increases exponentially with cell size, Omnipose displays a consistent error rate that

224   remains below 4% for all percentiles (Fig. 4b). Thus, Omnipose performance is

225   independent of cell size and shape, including those cells with complex, extended

226   morphologies (Fig. 4c,d).

227

228   **Omnipose permits sensitive detection of cellular intoxication**

229   Our laboratory recently described an interbacterial type VI secretion system-

230   delivered toxin produced by *Serratia proteamaculans*, Tre1[36]. We showed that this toxin

231   acts by ADP-ribosylating the essential cell division factor FtsZ; however, we were unable

232   to robustly evaluate the consequences of Tre1 intoxication on target cell morphology

233   owing to segmentation challenges. Here we asked whether Omnipose could permit

234   straightforward and sensitive detection of intoxication by Tre1. To this end, we incubated

235   *S. proteamaculans* wild-type or a control strain expressing inactive Tre1 (*tre1*^{E415Q}*)* with

236   target *E. coli* cells and imaged these mixtures after a fixed period of 20 hours. Owing to

237   the unique capabilities of Omnipose, we were able to include dense fields of view,

238   incorporating >300,000 cells in our analysis.

239   Among the cells identified by Omnipose, we found a small proportion were

240   elongated and much larger than typical bacteria (Fig. 5a,b and Extended Data Fig. 6a).

241   These cells were only detected in mixtures containing active Tre1, and the apparent

242   failure of the cells to septate is consistent with the known FtsZ-inhibitory activity of the

243   toxin. The *S. proteamaculans* strain background we employed in this work expresses the

244   green fluorescent protein. Corresponding fluorescence images allowed us to

245   unambiguously assign the enlarged cell population to *E. coli* (Fig. 5c). Next, we

246   subjected the same images to cell segmentation with StarDist, Cellpose, and MiSiC, the

247   three top-performing algorithms in our initial survey. Each of these algorithms fail to

248   identify this population of cells to high precision (Fig. 5d,e). Close inspection reveals

249   three distinct modes of failure (Fig. 5e and Extended Data Fig. 6b). In the case of

250   StarDist, elongated (non-star-convex) cells are split into multiple star-convex subsets that

251   do not span the entire cell. Cellpose detects entire elongated cells, but it breaks them up

252   into a multitude of smaller masks. Conversely, MiSiC detects all cells but fails to

253   properly separate them, thereby exaggerating the area measurement in many cases. Taken

254   together, these data illustrate how the enhanced cell segmentation performance of

255   Omnipose can facilitate unique insights into microbiological systems.

256

257   **Omnipose exhibits strong performance in non-bacterial segmentation tasks**

258   We have shown that the features we developed within Omnipose improved phase-

259   contrast bacterial segmentation performance beyond that of Cellpose. However, it is

260   possible that these features could hinder performance relative to Cellpose in other

261   imaging modalities or in segmentation tasks involving, for example, eukaryotic cells,

262   whole organisms, and cell-like objects. To test this, we trained Omnipose on the cyto2

263   dataset, a large collection of images and corresponding ground-truth annotations

264   submitted by users that expands upon the original cyto dataset of Cellpose[12,30]. We found

265   that Omnipose offers a modest improvement in performance relative to Cellpose on this

266   dataset (Fig. 5f and Extended Data Fig. 7a). Moreover, Omnipose achieved this

267   performance boost without compromising the segmentation rate (~1 image per second).

268   Encouraged by the strong performance of Omnipose on the cyto2 dataset, we next

269   sought to investigate its potential utility in a field far removed from microbiology. The

270   nematode *Caenorhabditis elegans* is a widely studied model organism with an overall

271   morphology grossly similar to elongated bacteria[37]. At just one millimeter in length,

272   intact *C. elegans* are often analyzed by microscopy in order to measure phenotypes;

273   therefore, there is significant interest in methods for their accurate segmentation to enable

274   tracking[38]. We obtained, annotated and trained Omnipose on two publicly available

275   microscopy datasets composed of *C. elegans* images: time-lapse frames from the Open

276   Worm Movement database[39] and frames containing fields of assorted live or dead *C.*

277   *elegans* from the BBBC010 dataset[40]. These images contain debris and are of

278   heterogenous quality, yet 82% of masks predicted by Omnipose match or exceed the 0.8

279   IoU threshold (Fig. 5g,h). Taken together with our findings on cyto2, we conclude that

280   Omnipose inherits and offers improvement upon the broad applicability of Cellpose.

281

282   **Discussion**

283   Confronted with the importance of segmentation accuracy to the success of work

284   within our own laboratory, we were motivated to characterize the performance of several

285   existing cell segmentation algorithms. Recent developments in deep learning have greatly

286   improved these algorithms; however, significant challenges remain[1,30]. Although isolated

287   cells without cell-to-cell contact can be segmented with high precision by any of the

288   packages we tested, segmentation becomes significantly more challenging when cells

289   form microcolonies, adopt irregular morphologies, or when fields are composed of cells

290   with multiple shapes and sizes. Such difficulties are compounded in time-lapse studies,

14

291   where the significance of segmentation errors often grows exponentially with time.

292   Experimental design can help mitigate certain segmentation challenges; however, the

293   recent emphasis on non-model organisms and microbial communities renders this an

294   increasingly undesirable solution[41].

295   This work provides the most comprehensive side-by-side quantitative comparison

296   of cell segmentation algorithm performance to-date. As expected, machine-learning-

297   based approaches outperform others, yet insights into general image segmentation

298   strategies can be gained from each of the methods we examined. Two of the six

299   algorithms we tested utilize traditional image thresholding and watershed segmentation:

300   Morphometrics and SuperSegger[13,23]. Each program tends to under-segment adjacent

301   cells and over-segment large cells, behaviors previously linked to thresholding and

302   watershed processes, respectively[1,42]. Given that SuperSegger was motivated at least in-

303   part to mitigate these issues, we postulate that traditional image segmentation approaches

304   are ultimately limited to specialized imaging scenarios. Although we classify MiSiC as a

305   DNN-based approach, this algorithm also relies on thresholding and watershed

306   segmentation to generate cell masks from its network output[15]. The network output of

307   MiSiC is more uniform than unfiltered phase contrast images, yet this pre-processing

308   does not fully abrogate the typical errors of thresholding and watershed segmentation.

309   We therefore conclude that, even when combined with neural networks as seen in MiSiC,

310   thresholding and watershed cannot be effectively used for general cell segmentation

311   tasks.

312   A successful DNN-based algorithm is composed of a robust, consistent neural

313   network output, and an appropriate mask reconstruction process based on this output. In

15

314   the case of Mask R-CNN, bounding boxes for each cell are predicted along with a

315   probability field that localizes a cell within its bounding box[43]. Masks are generated by

316   iterating over each box and thresholding the probability field. Despite the widespread

317   adoption of Mask R-CNN, we found this algorithm did not perform exceptionally well in

318   our study. Our results suggest that this is due to dense cell fields with overlapping

319   bounding boxes, a feature known to corrupt the training process and produce poor

320   network outputs for Mask R-CNN[44]. By contrast, the StarDist network makes robust

321   predictions, but it fails to assemble accurate cell masks because the cells in our dataset

322   are not well approximated by star-convex polygons[26]. The errors we encountered with

323   Cellpose can be attributed to both neural network output and mask reconstruction. In

324   Omnipose, we specifically addressed these two issues via the distance field and

325   suppressed Euler integration, respectively, yielding a remarkably precise and

326   generalizable image segmentation tool. Omnipose effectively leverages the strongest

327   features of several of the DNN approaches we tested, namely the distance field of

328   StarDist, the boundary field of MiSiC, and the mask reconstruction framework of

329   Cellpose.

330   We have designed Omnipose for use by typical research laboratories and we have

331   made its source code and training data publicly available. For images of bacteria under

332   phase contrast, researchers will not need to provide new ground truth data or retrain the

333   model. In this study, we emphasized morphological diversity, but we further accounted

334   for differences in optical features between bacterial strains, slide preparation techniques,

335   and microscope configurations. For example, the images in our ground-truth dataset

336   originate from four different researchers using distinct microscopes, objectives, sensors,

337   illumination sources, and acquisition settings. We further introduced extensive image

338   augmentations that simulate variations in image intensity, noise, gamma, clipping, and

339   magnification. Lastly, bacterial strains exhibit a wide range of intrinsic contrast and

340   internal structure, often exacerbated by antibiotic treatment or revealed by dense cell

341   packing. Internal structure can cause over-segmentation, so we included many cells with

342   this characteristic in our dataset.

343   We anticipate that the unprecedented performance of Omnipose may permit

344   access to information from microscopy images that was previously inaccessible. For

345   instance, images deriving from natural microbial communities could be accurately

346   characterized with regard to internal structure, autofluorescence, and morphology at the

347   single-cell level. This data could be used to estimate diversity, a novel methodology that

348   would complement existing sequencing-based metrics[45]. It is worth noting that

349   phenotypic diversity often exceeds genetic diversity[46]; therefore, even in a relatively

350   homogeneous collection of organisms, precise segmentation could allow classes

351   representing distinct states to be identified. A microscopy-based approach also offers the

352   opportunity to characterize spatial relationships between cells, information that is

353   exceptionally difficult to recover in most biomolecular assays.

354   **Methods**

355   **Phase contrast and fluorescence microscopy**

356   In-house imaging was performed on a Nikon Eclipse Ti-E wide-field epi-

357   fluorescence microscope, equipped with a sCMOS camera (Hamamatsu) and X-cite LED

358   for fluorescence imaging. We imaged through 60X and 100X 1.4 NA oil-immersion PH3

359   objectives. The microscope was controlled by NIS-Elements. Cell samples were spotted

360   on a 3% (w/v) agarose pad placed on a microscope slide. The microscope chamber was

361   heated to 30°C or 37°C when needed for time-lapse experiments.

362   Several images in our dataset were taken by two other laboratories using three

363   distinct microscope/camera configurations. The Brun lab provided images of *C.*

364   *crescentus* acquired on a Nikon Ti-E microscope equipped with a Photometrics Prime

365   95B sCMOS camera. Images were captured through a 60X Plan Apo λ 100X 1.45 NA oil

366   Ph3 DM objective. The Wiggins lab provided *E. coli* and *A. baylyi* time lapses from both

367   a Nikon Ti-E microscope as well as a custom-built tabletop microscope, both described in

368   previous studies[47,48].

369

370   *C. elegans* **data preparation**

371   We obtained a 1000-frame time lapse of *C. elegans* from the Wormpose[38] GitHub

372   (https://github.com/iteal/wormpose_data) adapted from the Open Worm Movement

373   database[39], which is inaccessible at the time of writing. We also utilized the Broad

374   Bioimage Benchmarking Collection set BBBC010[40] (https://bbbc.broadinstitute.org/c-

375   elegans-livedead-assay-0), a set of 100 images containing live and dead *C. elegans*.

376   These images were manually cropped to select regions of each image without *C. elegans*

18

377   overlaps. For both of these datasets, images were initially segmented with Omnipose to

378   select foreground, automatically cropped to select individual *C. elegans* or clusters of *C.*

379   *elegans*, and then packed into ensemble images for efficient annotation, training, and

380   testing following the same procedures described below for our bacterial datasets.

381

382   **Bacterial sample preparation**

383   To image antibiotic-induced phenotypes, cells were grown without antibiotics

384   overnight in LB, back-diluted, and spotted on agarose pads with 50µg/mL A22 or

385   10µg/mL cephalexin. Time lapses were captured of *E. coli* DH5α and *S. flexneri* M90T

386   growing on these pads. *E. coli* CS703-1 was back-diluted into LB containing 1µg/mL

387   aztreonam and spotted onto a pad without antibiotics[49]. Cells constitutively expressed

388   GFP to visualize cell boundaries.

389   *H. pylori* LSH100 grown with and without Aztreonam was provided by the

390   Salama lab[50,51]. Samples were fixed and stained with Alexaflour 488 to visualize the cell

391   membrane. Images were taken on LB pads. The typical technique of allowing the spot to

392   dry on the pad caused cells to curl up on themselves, so our images were taken by placing

393   the cover slip on the pad immediately after spotting and applying pressure to force out

394   excess media.

395   *C. crescentus* was cultivated and imaged by the Brun lab[52,53]. Cells were grown in

396   PYE, washed twice in water prior to 1:20 dilution in Hutner base-imidazole-buffered-

397   glucose-glutamate (HIGG media) and grown at 26°C for 72h. Cells were spotted on a 1%

398   agarose PYE pads prior to imaging.

399   *S. pristinaespiralis* NRRL 2958 was grown using the following media recipe:

400   Yeast extract 4g/L, Malt extract 10g/L, Dextrose 4g/L, Agar 20g/L. This media was used

401   to first culture the bacteria in liquid overnight and then on a pad under the microscope.

402   This strain forms aggregates in liquid media, so these aggregates were allowed to grow

403   for several hours on a slide in the heated microscope chamber until we could see

404   individual filaments extending from the aggregates. Fields of view were selected and

405   cropped to exclude cell overlaps. Autofluorescence was captured to aid in manual

406   segmentation.

407   Mixtures of *S. proteamaculans* attTn7::Km-gfp *tre1* or *tre1^{E415Q}* and *E. coli* were

408   spotted on a PBS pad to prevent further growth. Phase-contrast images of the cells were

409   acquired before and after a 20hr competition on a high-salt LB plate. Fluorescence

410   images in the GFP channel were also acquired to distinguish *S. proteamaculans* from

411   unlabeled *E. coli*.

412   All other individual strains in Table S1 were grown overnight, diluted 1:100 into

413   fresh LB media, and grown for 1-3 hours before imaging. Mixtures were made by

414   combining back-diluted cells roughly 1:1 by OD_{600}.

415

416   **Manual image annotation**

417   Manual annotation began with loading images into MATLAB, normalizing the

418   channels, registering the fluorescence channel(s) to brightfield (when applicable), and

419   producing boundary-enhanced versions of brightfield and fluorescence. Where possible,

420   fluorescence data was primarily used to define cell boundaries (not available in the *C.*

421   *elegans* dataset acquired online). In addition to a blank channel to store manual labels, all

422   processed phase and fluorescence images were then automatically loaded as layers into

423   an Adobe Photoshop document. We used 4-6 unique colors and the Pencil tool (for pixel-

424   level accuracy and no blending) to manually define object masks. Due to the 4-color

425   theorem[54], this limited palette was sufficient to clearly distinguish individual object

426   instances from each other during annotation. This color simplification is not found in any

427   segmentation GUI, and it enabled faster manual annotation by reducing the need to select

428   new colors. It also eliminated the confusion caused by the use of similar but distinct

429   colors in adjacent regions, which we suspect is the principal cause for the misplaced

430   mask pixels that we observed in other datasets (*e.g.,* cyto2).

431   The cell label layer was then exported as a PNG from Photoshop, read back into

432   MATLAB, and converted from the repeating N-color labels to a standard 16-bit integer

433   label matrix, where each object is assigned a unique integer from 1 to the number of cells

434   (background is 0). Because integer labels cannot be interpolated, we then performed a

435   non-rigid image registration of the brightfield channel to the binary label mask to achieve

436   better brightfield correlation to ground truth masks. All images in our ground-truth

437   dataset have been registered in this manner.

438

439   **Choosing Segmentation algorithms**

440   Three main factors contributed to the choice of algorithms highlighted in this

441   study: (*i*) specificity to bacterial phase contrast images, (*ii*) success and community

442   adoption, especially for bioimage segmentation, and (*iii*) feasibility of installation,

443   training, and use. SuperSegger, Morphometrics, and MiSiC were selected because they

444   specifically targeted the problem of bacterial phase contrast segmentation[15,23,55]. Packages

445   such as BactMAP, BacStalk, Cellprofiler, CellShape, ColiCoords, Cytokit,

446   MicroAnalyzer, MicrobeJ, Oufti, and Schnitzcells incorporate limited novel segmentation

447   solutions and instead aim to provide tools for single-cell analysis such as lineage tracing

448   and protein tracking[8,9,14,18-20,25,56-58]. Furthermore, the segmentation that these programs

449   perform depends broadly on thresholding and watershed techniques; therefore,

450   Morphometrics is a reasonable proxy for their segmentation capabilities. We were unable

451   to locate code or training data for BASCA[11]. Ilastik is a popular interactive machine-

452   learning tool for bioimage segmentation, but training it using a manual interface was not

453   feasible on a large and diverse dataset such as our own[21]. Among DNN approaches, Mask

454   R-CNN was selected because it is a popular architecture for handling typical image

455   segmentation tasks. It was also used in the segmentation and tracking package Usiigaci[24].

456   U-Net architectures have been implemented in a number of algorithms, including

457   DeLTA, PlantSeg, MiSiC, StarDist, and Cellpose[12,15,17,22,26]. DeLTA was not included in

458   this study because it operates similarly to MiSiC and was designed specifically for

459   mother machine microfluidics analysis. DeLTA 2.0 was recently released to additionally

460   segment confluent cell growth on agarose pads, but it remains quite similar to MiSiC in

461   implementation[59]. PlantSeg could, in principle, be trained on bacterial micrographs, but

462   we determined that its edge-focused design meant to segment bright plant cell wall

463   features would not offer any advancements over the remaining U-Net methods that we

464   tested.

465

466   **Training and tuning segmentation algorithms**

22

467   All segmentation algorithms have tunable parameters to optimize performance on

468   a given dataset. These include pre-processing such as image rescaling (often to put cells

469   into a particular pixel diameter range), contrast adjustment, smoothing, and noise

470   addition. Morphometrics and SuperSegger were manually tuned to give the best results

471   on our benchmarking dataset. The neural network component of SuperSegger was not

472   retrained on our data, as this is a heavily manual process involving toggling watershed

473   lines on numerous segmentation examples. DNN-based algorithms are automatically

474   trained using our dataset, and the scripts we used to do so are available in our GitHub

475   repository. We adapted our data for MiSiC by transforming our instance labels into

476   interior and boundary masks. Training documentation for MiSiC is not published.

477   Training and evaluation parameters for MiSiC were tuned according to correspondence

478   with the MiSiC authors. Cellpose and StarDist were trained with the default parameters

479   provided in their documentation. StarDist has an additional tool to optimize image pre-

480   processing parameters on our dataset, which we utilized.

481

482   **Evaluating segmentation algorithms**

483   All algorithms were evaluated on our benchmarking dataset with manually or

484   automatically optimized parameters. We provide both the raw segmentation results for all

485   test images by each tested algorithm as well as the models and model-training scripts

486   required to reproduce our results. Before evaluating IoU or JI, small masks at image

487   boundaries were removed for both the ground-truth and predicted masks. IoU and JI are

488   calculated on a per-image basis and, where shown, are averaged with equal weighting

489   over the image set or field of view.

23

490   Our new metric, the number of segmentation errors per cell, was calculated by

491   first measuring the fraction of each predicted cell that overlaps with each ground truth

492   cell. A predicted cell is assigned to a ground-truth cell if the overlap ratio is ≥ 0.75,

493   meaning that at least three quarters of the predicted cell lies within the ground-truth cell.

494   If several predicted cells are matched to a ground-truth cell, the number of surplus

495   matches is taken to be the number of segmentation errors. If no cells are matched to a

496   ground-truth cell, then the error is taken to be 1.

497

498   **Leveraging Omnipose to accelerate manual annotation**

499   Omnipose was periodically trained on our growing dataset to make initial cell

500   labels. These were converted into an N-color representation and loaded into Photoshop

501   for manual correction. A subset of our cytosol GFP channels were sufficient for training

502   Omnipose to segment based on fluorescence, and the resulting trained model enabled

503   higher-quality initial cell labels for GFP-expressing samples than could be achieved from

504   intermediate phase contrast models (*e.g., V. cholerae*).

505

506   **Defining the Omnipose prediction classes**

507   Omnipose predicts four classes: two flow components, the distance field, and a

508   boundary field. Our distance field is found by solving the eikonal equation

$$\left|\vec{\nabla}\phi(\vec{x})\right| = \frac{1}{f(\vec{x})}$$

510   where f represents the speed at a point $\vec{x}$. The Godunov upwind discretization of the

511   eikonal equation is

24

512
$$\left(\frac{\max\left(\phi_{i,j}-\min\left(\phi_{i-1,j},\phi_{i+1,j}\right),0\right)}{\Delta x}\right)^2 + \left(\frac{\max\left(\phi_{i,j}-\min\left(\phi_{1,j-1},\phi_{i,j+1}\right),0\right)}{\Delta y}\right)^2 = \frac{1}{f_{i,j}}$$

513   Our solution to this equation is based on the Improved FIM Algorithm 1.1 of[34], as

514 follows. Our key contribution to this algorithm is the addition of ordinal sampling to

515 boost both convergence and smoothness of the final distance field.

516   *2D update function for $\phi_{i,j}$ on a cartesian grid*

517   1. Find neighboring points for cardinal axes ($\Delta x = \Delta y = \delta$):

518
$$\phi^{\text{minx}} = \min\left(\phi_{i-1,j},\phi_{i+1,j}\right), \qquad \phi^{\text{miny}} = \min\left(\phi_{i,j-1},\phi_{i,j+1}\right)$$

519   2. Find neighboring points for ordinal axes ($\hat{x}\cdot\hat{a} = \hat{y}\cdot\hat{b} = \frac{\sqrt{2}}{2}, \frac{\Delta a}{\Delta x} = \frac{\Delta b}{\Delta y} = \sqrt{2}\delta$):

520
$$\phi^{\text{mina}} = \min\left(\phi_{i-1,j-1},\phi_{i+1,j+1}\right), \qquad \phi^{\text{minb}} = \min\left(\phi_{i+1,j-1},\phi_{i-1,j+1}\right)$$

521   3. Calculate update along cardinal axes:

522   **if** $\left|\phi^{\text{minx}}-\phi^{\text{miny}}\right| > \frac{\sqrt{2}\delta}{f_{i,j}}$:

523
$$U^{xy} = \min\left(\phi^{\text{minx}},\phi^{\text{miny}}\right) + \frac{\delta}{f_{i,j}}$$

524   **else**:

525
$$U^{xy} = \frac{1}{2}\left(\phi^{\text{minx}} + \phi^{\text{miny}} + \sqrt{2\left(\frac{\delta}{f_{i,j}}\right)^2 - (\phi^{\text{minx}}-\phi^{\text{miny}})^2}\right)$$

526   4. Calculate update along ordinal axes:

527   **if** $\left|\phi^{\text{mina}}-\phi^{\text{minb}}\right| > \frac{2\delta}{f_{i,j}}$:

528
$$U^{ab} = \min\left(\phi^{\text{mina}},\phi^{\text{minb}}\right) + \frac{\sqrt{2}\delta}{f_{i,j}}$$

529   **else**:

530
$$U^{ab} = \frac{1}{2}\left(\phi^{\text{mina}} + \phi^{\text{minb}} + \sqrt{4\left(\frac{\delta}{f_{i,j}}\right)^2 - (\phi^{\text{mina}}-\phi^{\text{minb}})^2}\right)$$

531   5. Update with geometric mean:

532
$$\phi_{i,j} = \sqrt{U^{xy}U^{ab}}$$

25

533   This update rule is repeated until convergence (Extended Data Fig. 5). We take

534    $\delta = f_{i,j}$ to obtain the signed distance field used in Omnipose. The flow field components

535   are defined by the normalized gradient of this distance field ϕ. The boundary field is

536   defined by points satisfying $0 < \phi < 1$. For network prediction, the boundary map is

537   converted to the logits (inverse sigmoid) representation, such that points in the range

538    $[0,1]$ are mapped to $[-5,5]$. For consistent value ranges across prediction classes, the

539   flow components are multiplied by 5 and all background values of the distance field ($\phi =$

540   0) are set to -5.

541

542   **Omnipose network architecture**

543   The DNN used for Omnipose is a minor modification of that used in Cellpose: a

544   U-net architecture with two residual blocks per scale, each with two convolutional

545   layers[12]. Omnipose introduces a dropout layer before the densely connected layer[60],

546   which we incorporated into the shared Cellpose and Omnipose architecture moving

547   forward. However, Cellpose models utilized in this study are trained without dropout.

548

549   **Rescaling flow field by divergence**

550   During training, the ground truth data is augmented by a random affine

551   transformation. The original implementation, and the one which yields the best results,

552   linearly interpolates the transformed field. This reduces the magnitude of the otherwise

553   normalized field in regions of divergence, *i.e.,* at boundaries and skeletons. A

554   renormalized field (obtained either from the transformed field or as the normalized

555   gradient of the transformed heat distribution) often has artifacts at cell boundaries and

556 skeletons, so the interpolated field effectively reduces the influence of these artifacts on

557 training. We reason that this feature explains the superior performance of interpolated

558 field training over renormalized fields, despite the latter being the nominal goal of the

559 algorithm.

560 Pixels at cell boundaries, however, consequently do not move far (less than 1px)

561 under Euler integration due to the low magnitude of the predicted field at cell boundaries.

562 Our solution in Omnipose is to rescale the flow field by the magnitude of the divergence.

563 The divergence is most positive at the cell boundaries (where pixels need to move) and

564 most negative at cell skeletons (where pixels need to stop). We therefore rescale the

565 divergence from 0 to 1 and multiply the normalized flow field by this new magnitude

566 map. This forces boundary pixels of neighboring cells to quickly diverge and allow for

567 accurate pixel clustering to obtain the final segmentation.

568

569 **Novel diameter metric**

570 The size models of Cellpose are trained to estimate the average cell 'diameter',

571 taken to be the diameter of the circle of equivalent area:

572
$$d = 2\mathrm{R} = 2\sqrt{\frac{A}{\pi}} \qquad (*)$$

573 This metric as a basis for rescaling is problematic when cells are growing in

574 length but not width (Extended Data Fig. 7). Log-phase bacterial cell area grows

575 exponentially with time, and so too does the scale factor, eventually resulting in a

576 rescaled image that is too small for Cellpose to segment.

577   The average of the distance field, however, does not change for filamentous

578 bacteria, as the width – and therefore the distance to the closest boundary – remains

579 constant. To define a formula consistent with the previous definition in the case of a

580 circular cell, we consider mean of the distance field over the cell:

581
$$\bar{\phi} = \frac{1}{\pi R^2} \int_0^{2\pi} \int_0^R (R - r) r\, dr\, d\theta = \frac{1}{\pi R^2} \left(\frac{\pi}{3} R^3 \right) = \frac{R}{3}$$

582   This allows us to define a new 'effective diameter' as

583
$$d = 2R = 6\bar{\phi} \qquad\qquad (**)$$

584   Aside from agreeing with the previous scaling method $(*)$ for round

585 morphologies, this definition exhibits excellent consistency across time (Extended Data

586 Fig. 7). This consistency is also critical for training on datasets with wide distributions in

587 cell areas that require rescaling, such as the Cellpose datasets. Finally, the raw distance

588 field output of Omnipose can directly be used directly in $(**)$ to estimate average cell

589 diameter, which is used in our code to automatically toggle on features that improve

590 mask reconstruction performance for small cells.

591

592 **Gamma augmentation**

593   To make the network robust against changes in exposure/contrast, the training

594 images are now raised to a random power (gamma) between 0.5 and 1.25, simulating the

595 varying levels of contrast that are observed experimentally with different light sources,

596 objectives, and exposure times.

597

598

599

600 **Alleviating class imbalance**

601   Class imbalance remains a challenge in many machine learning applications[61]. In

602 our dataset, foreground pixels (cells) take up anywhere from 1 to 75 percent of a given

603 training image, with the rest being background pixels that the network must only learn to

604 ignore (*i.e.*, assign a constant output of -5 for distance and boundary logits). We

605 implemented several changes to the loss function to emphasize foreground objects,

606 including weighting by the distance field and averaging some loss terms only over

607 foreground pixels. Our training augmentation function also attempts many random crop

608 and resizing passes until a field of view with foreground pixels is selected (this may take

609 several attempts for sparse images, but adds very little time to training).

610

611 **Image normalization**

612   To manage different image exposure levels, Cellpose automatically rescales

613 images such that pixels in the 1st percentile of intensity are set to 0 and those in the 99th

614 percentile are sent to 1. This percentile rescaling is preferred over blind min-max

615 rescaling because bubbles or glass can cause small bright spots in the image. However,

616 we found that images containing single cells (low intensity) in a wide field of media

617 (high intensity) would become badly clipped due to the foreground-background class

618 imbalance. To solve this, we changed the percentile range from 0.01 to 99.99.

619

620 **Data availability**

621   Ground truth images and labels generated for this study are hosted on the Cellpose

622   website (http://www.cellpose.org/dataset_omnipose) and listed on the Papers With Code

623   database (https://paperswithcode.com/dataset/bpcis).

624

625   **Code availability**

626   For install instructions, source code, and all Python and MATLAB scripts generated for

627   this study, see our GitHub repository at https://github.com/kevinjohncutler/omnipose.

Acknowledgements

The authors wish to thank members of the Mougous and Wiggins laboratories for helpful

suggestions, See-Yeun Ting for assistance with experiments, Teresa Lo for assistance

with image acquisition, Sophie Sichel and Nina Salama lab for growing, fixing, and

staining *H. pylori* samples for in-house imaging, and David Kysela, Maxime Jacq and

Yves Brun for providing *C. crescentus* images. This work was supported by the NIH

(AI080609 to JDM, GM128191 to PAW, T32GM008268 to KJC). JDM is an HHMI

Investigator.

Competing interests

The authors declare no competing interests.

Author contributions

KJC, PAW and JDM conceived the study. KJC performed experiments, analyzed data,

and wrote the code. KJC, PAW, and JDM wrote the manuscript. CS edited the

manuscript and assisted in code development.

Author Information

Correspondence and requests for materials should be addressed to J.D.M.

(mougous@u.washington.edu) or P.A.W. (pwiggins@uw.edu).

649 **References**

650 1 Jeckel, H. & Drescher, K. Advances and opportunities in image analysis of
651 bacterial cells and communities. *FEMS Microbiol Rev* **45**,
652 doi:10.1093/femsre/fuaa062 (2021).

653 2 Bali, A. & Singh, S. N. in *IEEE Xplore*   113-120 (IEEE, 2015).

654 3 Lucas, A. M. *et al*. Open-source deep-learning software for bioimage
655 segmentation. *Mol Biol Cell* **32**, 823-829, doi:10.1091/mbc.E20-10-0660 (2021).

656 4 Kysela, D. T., Randich, A. M., Caccamo, P. D. & Brun, Y. V. Diversity Takes
657 Shape: Understanding the Mechanistic and Adaptive Basis of Bacterial
658 Morphology. *PLoS Biol* **14**, e1002565, doi:10.1371/journal.pbio.1002565 (2016).

659 5 Jones, S. E. & Elliot, M. A. 'Exploring' the regulation of Streptomyces growth and
660 development. *Curr Opin Microbiol* **42**, 25-30, doi:10.1016/j.mib.2017.09.009
661 (2018).

662 6 Caccamo, P. D. & Brun, Y. V. The Molecular Basis of Noncanonical Bacterial
663 Morphology. *Trends Microbiol* **26**, 191-208, doi:10.1016/j.tim.2017.09.012
664 (2018).

665 7 Behera, B. *et al*. Emerging technologies for antibiotic susceptibility testing.
666 *Biosens Bioelectron* **142**, 111552, doi:10.1016/j.bios.2019.111552 (2019).

667 8 Paintdakhi, A. *et al*. Oufti: an integrated software package for high-accuracy,
668 high-throughput quantitative microscopy analysis. *Molecular microbiology* **99**,
669 767-777, doi:10.1111/mmi.13264 (2016).

670 9 Ducret, A., Quardokus, E. M. & Brun, Y. V. MicrobeJ, a tool for high throughput
671 bacterial cell detection and quantitative analysis. *Nat Microbiol* **1**, 16077,
672 doi:10.1038/nmicrobiol.2016.77 (2016).

673 10 Tropini, C., Earle, K. A., Huang, K. C. & Sonnenburg, J. L. The Gut Microbiome:
674 Connecting Spatial Organization to Function. *Cell Host Microbe* **21**, 433-442,
675 doi:10.1016/j.chom.2017.03.010 (2017).

676 11 Balomenos, A. D. *et al*. Image analysis driven single-cell analytics for systems
677 microbiology. *BMC Syst Biol* **11**, 43, doi:10.1186/s12918-017-0399-z (2017).

678 12 Stringer, C., Wang, T., Michaelos, M. & Pachitariu, M. Cellpose: a generalist
679 algorithm for cellular segmentation. *Nature methods* **18**, 100-106,
680 doi:10.1038/s41592-020-01018-x (2021).

681 13 Stylianidou, S., Brennan, C., Nissen, S. B., Kuwada, N. J. & Wiggins, P. A.
682 SuperSegger: robust image segmentation, analysis and lineage tracking of

683   bacterial cells. *Molecular microbiology* **102**, 690-700, doi:10.1111/mmi.13486
684   (2016).

685 14 van Raaphorst, R., Kjos, M. & Veening, J. W. BactMAP: An R package for
686   integrating, analyzing and visualizing bacterial microscopy data. *Molecular*
687   *microbiology* **113**, 297-308, doi:10.1111/mmi.14417 (2020).

688 15 Panigrahi, S. *et al*. Misic, a general deep learning-based method for the high-
689   throughput cell segmentation of complex bacterial communities. *Elife* **10**,
690   doi:10.7554/eLife.65151 (2021).

691 16 Bannon, D. *et al*. DeepCell Kiosk: scaling deep learning-enabled cellular image
692   analysis with Kubernetes. *Nature methods* **18**, 43-45, doi:10.1038/s41592-020-
693   01023-0 (2021).

694 17 Lugagne, J. B., Lin, H. & Dunlop, M. J. DeLTA: Automated cell segmentation,
695   tracking, and lineage reconstruction using deep learning. *PLoS computational*
696   *biology* **16**, e1007673, doi:10.1371/journal.pcbi.1007673 (2020).

697 18 Smit, J. H., Li, Y., Warszawik, E. M., Herrmann, A. & Cordes, T. ColiCoords: A
698   Python package for the analysis of bacterial fluorescence microscopy data. *PLoS*
699   *One* **14**, e0217524, doi:10.1371/journal.pone.0217524 (2019).

700 19 Czech, E., Aksoy, B. A., Aksoy, P. & Hammerbacher, J. Cytokit: a single-cell
701   analysis toolkit for high dimensional fluorescent microscopy imaging. *BMC*
702   *Bioinformatics* **20**, 448, doi:10.1186/s12859-019-3055-3 (2019).

703 20 McQuin, C. *et al*. CellProfiler 3.0: Next-generation image processing for biology.
704   *PLoS Biol* **16**, e2005970, doi:10.1371/journal.pbio.2005970 (2018).

705 21 Berg, S. *et al*. ilastik: interactive machine learning for (bio)image analysis. *Nature*
706   *methods* **16**, 1226-1232, doi:10.1038/s41592-019-0582-9 (2019).

707 22 Wolny, A. *et al*. Accurate and versatile 3D segmentation of plant tissues at
708   cellular resolution. *Elife* **9**, doi:10.7554/eLife.57613 (2020).

709 23 Ursell, T. *et al*. Rapid, precise quantification of bacterial cellular dimensions
710   across a genomic-scale knockout library. *BMC Biol* **15**, 17, doi:10.1186/s12915-
711   017-0348-8 (2017).

712 24 Tsai, H. F., Gajda, J., Sloan, T. F. W., Rares, A. & Shen, A. Usiigaci: Instance-
713   aware cell tracking in stain-free phase contrast microscopy enabled by machine
714   learning. *SoftwareX* **9**, 230-237, doi:https://doi.org/10.1016/j.softx.2019.02.007
715   (2019).

716 25 Reiner, J., Azran, G. & Hyams, G. MicroAnalyzer: A Python Tool for Automated
717   Bacterial Analysis with Fluorescence Microscopy. *arXiv*,
718   doi:https://arxiv.org/abs/2009.12684 (2020).

719 26   Schmidt, U. *et al*. *Cell Detection with Star-Convex Polygons*. (2018).

720 27   He, K., Gkioxari, G., Dollar, P. & Girshick, R. Mask R-CNN. *arXiv*,
721   doi:https://arxiv.org/abs/1703.06870 (2018).

722 28   Shal, K. & Choudhry, M. S. Evolution of Deep Learning Algorithms for MRI-
723   Based Brain Tumor Image Segmentation. *Crit Rev Biomed Eng* **49**, 77-94,
724   doi:10.1615/CritRevBiomedEng.2021035557 (2021).

725 29   Bean, G. J. *et al*. A22 disrupts the bacterial actin cytoskeleton by directly binding
726   and inducing a low-affinity state in MreB. *Biochemistry* **48**, 4852-4857,
727   doi:10.1021/bi900014d (2009).

728 30   Laine, R. F., Arganda-Carreras, I., Henriques, R. & Jacquemet, G. Avoiding a
729   replication crisis in deep-learning-based bioimage analysis. *Nature methods* **18**,
730   1136-1144, doi:10.1038/s41592-021-01284-3 (2021).

731 31   Taha, A. A. & Hanbury, A. Metrics for evaluating 3D medical image
732   segmentation: analysis, selection, and tool. *BMC Med Imaging* **15**, 29,
733   doi:10.1186/s12880-015-0068-x (2015).

734 32   Lu, W. *et al*. Unsupervised Sequential Outlier Detection With Deep Architectures.
735   *IEEE Trans Image Process* **26**, 4321-4330, doi:10.1109/TIP.2017.2713048
736   (2017).

737 33   Sethian, J. A. & Vladimirsky, A. Ordered upwind methods for static Hamilton-
738   Jacobi equations. *Proc Natl Acad Sci U S A* **98**, 11069-11074,
739   doi:10.1073/pnas.201222998 (2001).

740 34   Huang, Y. Improved Fast Iterative Algorithm for Eikonal Equation for GPU
741   Computing. *arXiv*, doi:http://arXiv:2106.15869v3 (2021).

742 35   Ester, M., Kreigel, H. P., Sander, J. & Xu, X. A density-based algorithm for
743   discovering clusters in large spatial databases with noise. doi:10.1.1.121.9220
744   (1996).

745 36   Ting, S. Y. *et al*. Bifunctional Immunity Proteins Protect Bacteria against FtsZ-
746   Targeting ADP-Ribosylating Toxins. *Cell* **175**, 1380-1392,
747   doi:10.1016/j.cell.2018.09.037 (2018).

748 37   Girard, L. R. *et al*. WormBook: the online review of Caenorhabditis elegans
749   biology. *Nucleic Acids Res* **35**, D472-475, doi:10.1093/nar/gkl894 (2007).

750 38   Hebert, L., Ahamed, T., Costa, A. C., O'Shaughnessy, L. & Stephens, G. J.
751   WormPose: Image synthesis and convolutional networks for pose estimation in C.
752   elegans. *PLoS computational biology* **17**, e1008914,
753   doi:10.1371/journal.pcbi.1008914 (2021).

754   39   Javer, A. *et al*. An open-source platform for analyzing and sharing worm-behavior
755   data. *Nature methods* **15**, 645-646, doi:10.1038/s41592-018-0112-1 (2018).

756   40   Ljosa, V., Sokolnicki, K. L. & Carpenter, A. E. Annotated high-throughput
757   microscopy image sets for validation. *Nature methods* **9**, 637,
758   doi:10.1038/nmeth.2083 (2012).

759   41   Cusick, J. A., Wellman, C. L. & Demas, G. E. The call of the wild: using non-
760   model systems to investigate microbiome-behaviour relationships. *J Exp Biol* **224**,
761   doi:10.1242/jeb.224485 (2021).

762   42   Wang, Z. Cell Segmentation for Image Cytometry: Advances, Insufficiencies, and
763   Challenges. *Cytometry A* **95**, 708-711, doi:10.1002/cyto.a.23686 (2019).

764   43   He, C. *et al*. Genome-resolved metagenomics reveals site-specific diversity of
765   episymbiotic CPR bacteria and DPANN archaea in groundwater ecosystems. *Nat*
766   *Microbiol* **6**, 354-365, doi:10.1038/s41564-020-00840-5 (2021).

767   44   Looi, S. *rotated_maskrcnn*, <https://github.com/mrlooi/rotated_maskrcnn>
768   (2019).

769   45   Bharti, R. & Grimm, D. G. Current challenges and best-practice protocols for
770   microbiome analysis. *Brief Bioinform* **22**, 178-193, doi:10.1093/bib/bbz155
771   (2021).

772   46   Smits, W. K., Kuipers, O. P. & Veening, J. W. Phenotypic variation in bacteria:
773   the role of feedback regulation. *Nat Rev Microbiol* **4**, 259-271,
774   doi:10.1038/nrmicro1381 (2006).

775   47   Bailey, J. *et al*. Essential gene deletions producing gigantic bacteria. *PLoS*
776   *genetics* **15**, e1008195, doi:10.1371/journal.pgen.1008195 (2019).

777   48   Cass, J. A., Stylianidou, S., Kuwada, N. J., Traxler, B. & Wiggins, P. A. Probing
778   bacterial cell biology using image cytometry. *Molecular microbiology* **103**, 818–
779   828, doi:10.1111/mmi.13591 (2017).

780   49   Meberg, B. M., Sailer, F. C., Nelson, D. E. & Young, K. D. Reconstruction of
781   Escherichia coli mrcA (PBP 1a) mutants lacking multiple combinations of
782   penicillin binding proteins. *J Bacteriol* **183**, 6148-6149,
783   doi:10.1128/JB.183.20.6148-6149.2001 (2001).

784   50   Lowenthal, A. C. *et al*. Functional analysis of the Helicobacter pylori flagellar
785   switch proteins. *J Bacteriol* **191**, 7147-7156, doi:10.1128/JB.00749-09 (2009).

786   51   Taylor, J. A. *et al*. Distinct cytoskeletal proteins define zones of enhanced cell
787   wall synthesis in Helicobacter pylori. *Elife* **9**, doi:10.7554/eLife.52482 (2020).

788   52   Evinger, M. & Agabian, N. Envelope-associated nucleoid from Caulobacter
789   crescentus stalked and swarmer cells. *J Bacteriol* **132**, 294-301,
790   doi:10.1128/jb.132.1.294-301.1977 (1977).

791   53   Caccamo, P. D., Jacq, M., VanNieuwenhze, M. S. & Brun, Y. V. A Division of
792   Labor in the Recruitment and Topological Organization of a Bacterial
793   Morphogenic Complex. *Curr Biol* **30**, 3908-3922 e3904,
794   doi:10.1016/j.cub.2020.07.063 (2020).

795   54   Robertson, N., Sanders, D. P., Seymour, P. & Thomas, R. A new proof of the
796   four-colour theorem. *Electron. Res. Announc. Amer. Math. Soc.* ,
797   doi:https://doi.org/10.1090/S1079-6762-96-00003-0 (1996).

798   55   Stylianidou, S., Brennan, C., Nissen, S. B., Kuwada, N. J. & Wiggins, P. A.
799   SuperSegger: robust image segmentation, analysis and lineage tracking of
800   bacterial cells. *Molecular microbiology* **102**, 690–700, doi:10.1111/mmi.13486
801   (2016).

802   56   Hartmann, R., van Teeseling, M. C. F., Thanbichler, M. & Drescher, K. BacStalk:
803   A comprehensive and interactive image analysis software tool for bacterial cell
804   biology. *Molecular microbiology* **114**, 140-150, doi:10.1111/mmi.14501 (2020).

805   57   Goni-Moreno, A., Kim, J. & de Lorenzo, V. CellShape: A user-friendly image
806   analysis tool for quantitative visualization of bacterial cell factories inside.
807   *Biotechnol J* **12**, doi:10.1002/biot.201600323 (2017).

808   58   Young, J. W. *et al.* Measuring single-cell gene expression dynamics in bacteria
809   using fluorescence time-lapse microscopy. *Nature protocols* **7**, 80-88,
810   doi:10.1038/nprot.2011.432 (2011).

811   59   O'Connor, O. M., Alnahhas, R. N., Lugagne, J. B. & Dunlop, M. J. DeLTA 2.0:
812   A deep learning pipeline for quantifying single-cell spatial and temporal
813   dynamics. *bioRxiv*, doi:https://doi.org/10.1101/2021.08.10.455795 (2021).

814   60   Srivastava, N., Hinton, G., Krizhevsky, A., Sutskever, I. & Salakhutdinov, R.
815   Dropout: a simple way to prevent neural networks from overfitting. *The Journal*
816   *of Machine Learning Research* **15**, 1929-1958 (2014).

817   61   Kaur, H., Pannu, H. S. & Malhi, A. K. A Systematic Review on Imbalanced Data
818   Challenges in Machine Learning: Applications and Solutions. *ACM Computing*
819   *Surveys* **52**, 1-36, doi:https://doi.org/10.1145/3343440 (2019).

820   62   Meberg, B. M., Sailer, F. C., Nelson, D. E. & Young, K. D. Reconstruction of
821   Escherichia coli mrcA (PBP 1a) mutants lacking multiple combinations of
822   penicillin binding proteins. *J Bacteriol* **183**, 6148–6149,
823   doi:10.1128/JB.183.20.6148-6149.2001 (2001).

824   63   Barbe, V. *et al*. Unique features revealed by the genome sequence of
825   Acinetobacter sp. ADP1, a versatile and naturally transformation competent
826   bacterium. *Nucleic Acids Res* **32**, 5766-5779, doi:10.1093/nar/gkh910 (2004).

827   64   Yu, Y. *et al*. Genomic patterns of pathogen evolution revealed by comparison of
828   Burkholderia pseudomallei, the causative agent of melioidosis, to avirulent
829   Burkholderia thailandensis. *BMC microbiology* **6**, 46 (2006).

830   65   Allue-Guardia, A., Echazarreta, M., Koenig, S. S. K., Klose, K. E. & Eppinger,
831   M. Closed Genome Sequence of Vibrio cholerae O1 El Tor Inaba Strain A1552.
832   *Genome Announc* **6**, doi:10.1128/genomeA.00098-18 (2018).

833   66   Stover, C. K. *et al*. Complete genome sequence of Pseudomonas aeruginosa
834   PA01, an opportunistic pathogen. *Nature* **406**, 959–964 (2000).

835
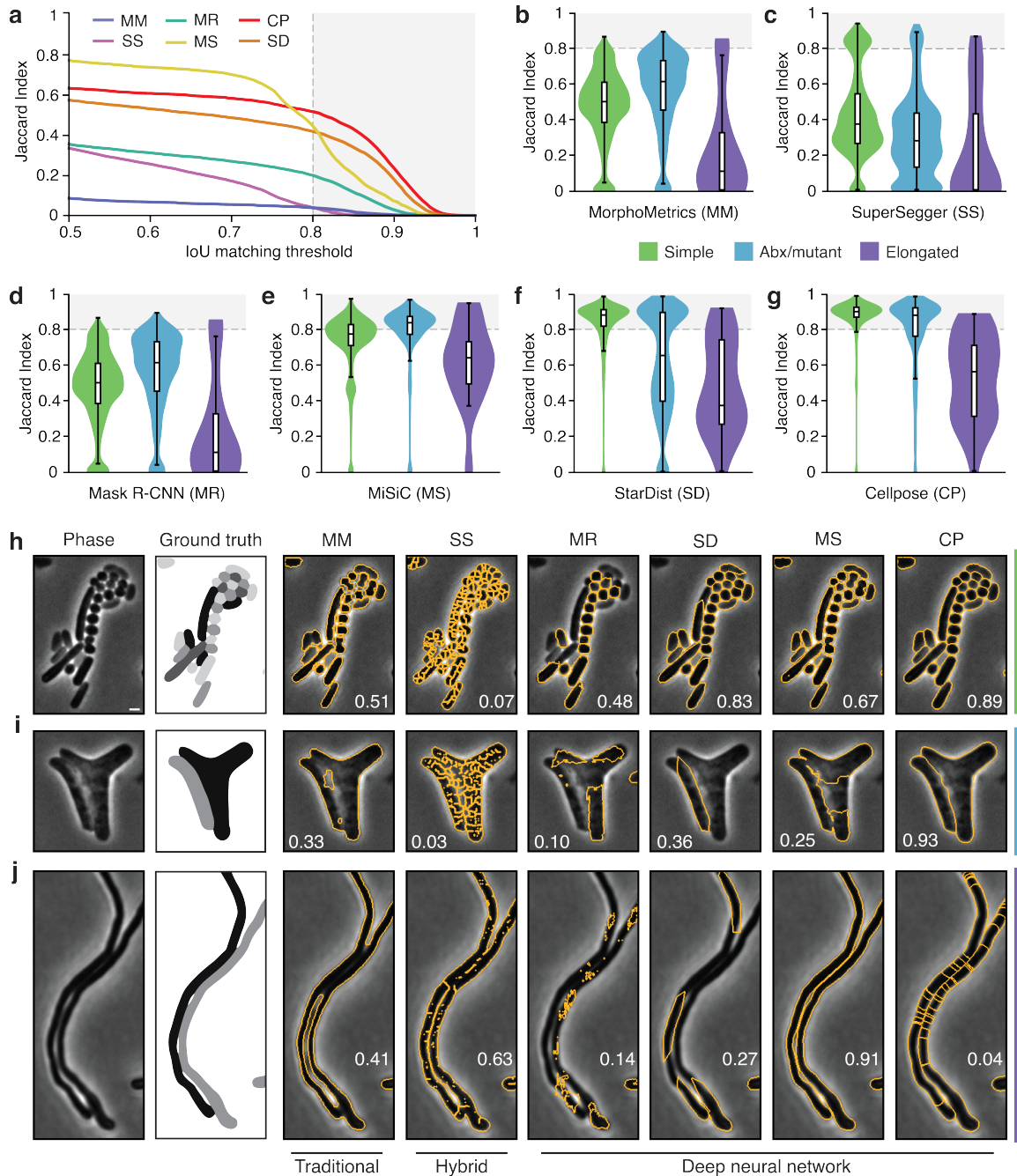
Fig. 1 | Quantitative comparison of segmentation methods distinguishes Cellpose as a high performing algorithm. (**a-g**) Comparison of segmentation algorithm performance on our test dataset. (**a**) Overall performance measured by Jaccard Index (JI). The JI was calculated at the image level and values averaged across the dataset are displayed. Algorithm abbreviations defined in B-G. (**b-g**) Algorithm performance partitioned by cell type (Simple, n=12,869; Abx/mutant, n=6,138; Elongated, n=46). Images were sorted into types as defined in Supplemental Table 1 (Abx, antibiotic). (**h-j**) Representative micrographs of cell type partitions analyzed in B-G, indicated by vertical bars at right. Ground-truth masks and predicted mask outlines generated by the indicated algorithm are displayed. Mean matched IoU values for cells shown are displayed within each micrograph. Bacteria displayed are (H) *Vibrio cholerae*, *Pseudomonas aeruginosa*, *Bacillus subtilis*, *Staphylococcus aureus*, (I) aztreonam-treated *Escherichia coli* CS703-1, and (J) *Streptomyces pristinaespiralis*. All images scaled equivalently; scale bar is 1mm.

38
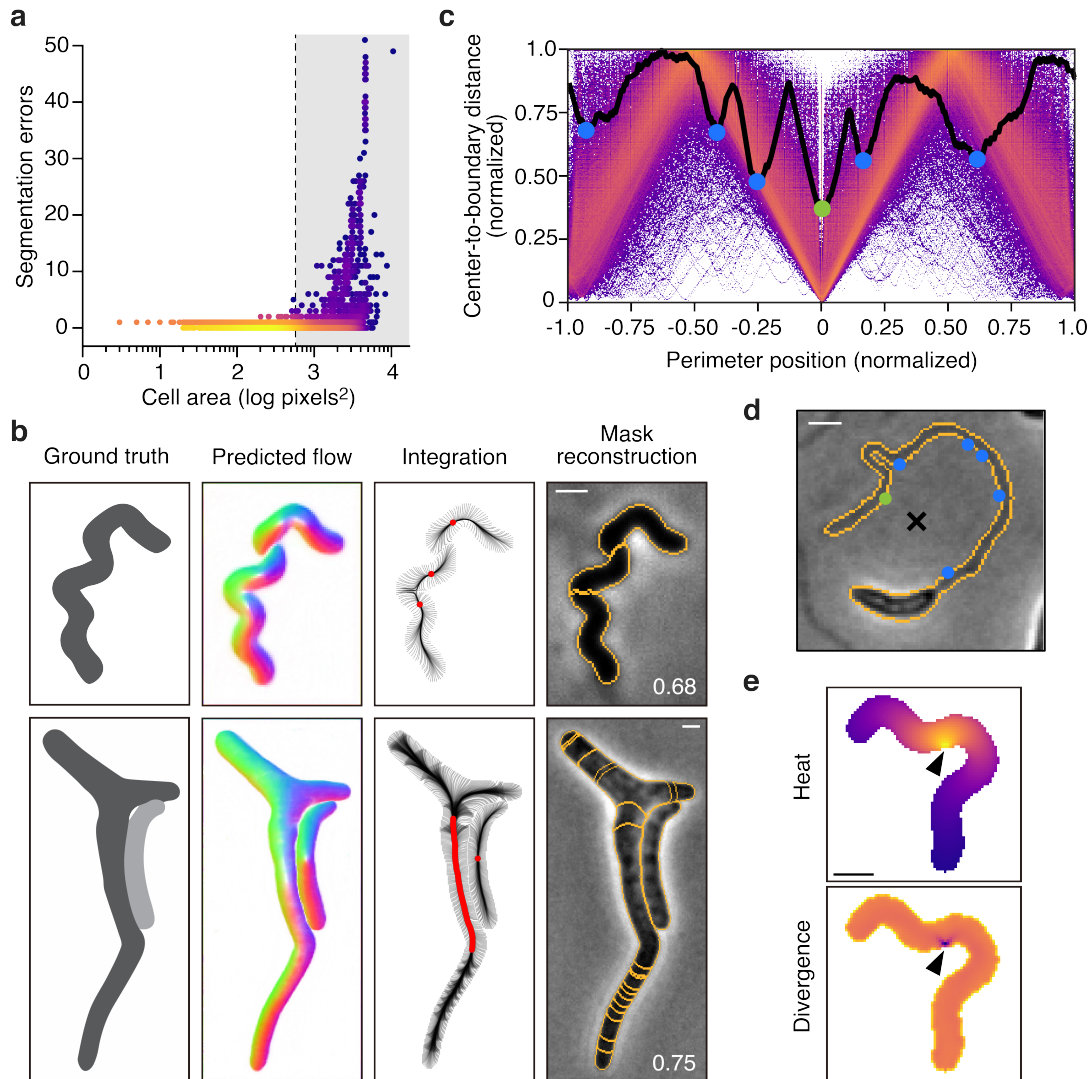
Fig. 2 | Cellpose over-segments extended, anisotropic cells. (**a**) Single-cell analysis of segmentation error as a function of cell area. Color represents density on a log scale. Gray box represents the top quartile of cell areas. (**b**) Representative examples exhibiting problematic flow fields. Corresponding boundary pixel trajectories are shown in black and final pixel locations in red. Predicted mask overlays are shown with mean matched IoU values. (**c**) Analysis of stochastic center-to-boundary distances. Distance from the center (median pixel coordinate) to each boundary pixel is normalized to a maximum of 1. Position along the boundary is normalized from -1 to 1 and centered on the point closest to the median pixel. Center-to-boundary for the cell in panel D is highlighted in black. (**d**) Representative cell with median coordinate outside the cell body (black X). Cellpose projects this point to the global minima of this function (green dot), but several other local minima exist (blue dots). (**e**) The heat distribution resulting from a projected cell center (black arrow). The normalized gradient corresponds to the divergence shown. Bacteria displayed are (a,e) *Helicobacter pylori*, (b) *Escherichia coli* CS703-1, both treated with aztreonam, and (d) *Caulobacter crescentus* grown in HIGG media. Scale bars are 1 μm.
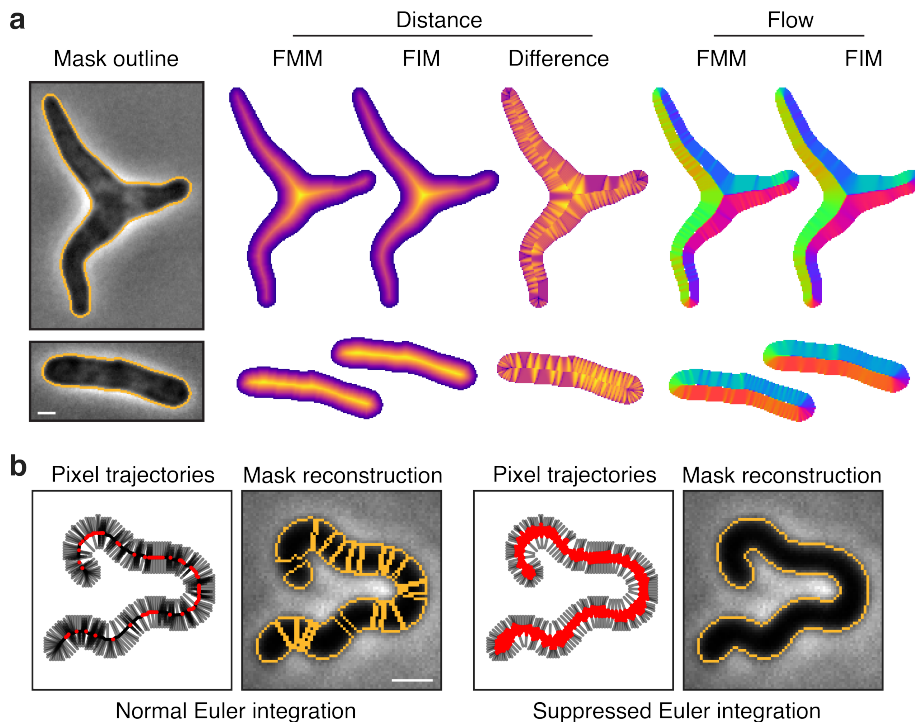
Fig. 3 | Core innovations of Omnipose. (**a**) Comparison of distance field algorithms and corresponding flow fields. Fast Marching Method (FMM) produces ridges in the distance field resulting from pixelation on the cell mask boundary. Our smooth FIM algorithm minimizes these features. The difference image (FIM – FMM) highlights artifacts in the FMM method. Flow fields are calculated as the normalized gradient of the distance field. Boundary pixelation affects the FMM flow field deep into the cell, regardless of cell size. (**b**) Comparison of mask reconstruction algorithms on a smooth flow field (not shown). Left: boundary pixel trajectories and resulting mask outlines from standard Euler integration. Right: Trajectories and mask outlines under suppressed Euler integration. Red dots indicate the final positions of all cell pixels, not only the boundary pixels for which trajectories are displayed. Bacteria displayed are (a) *Escherichia coli* CS703-1 and (b) and *Helicobacter pylori*, both treated with aztreonam. Scale bars are 1 μm.

40
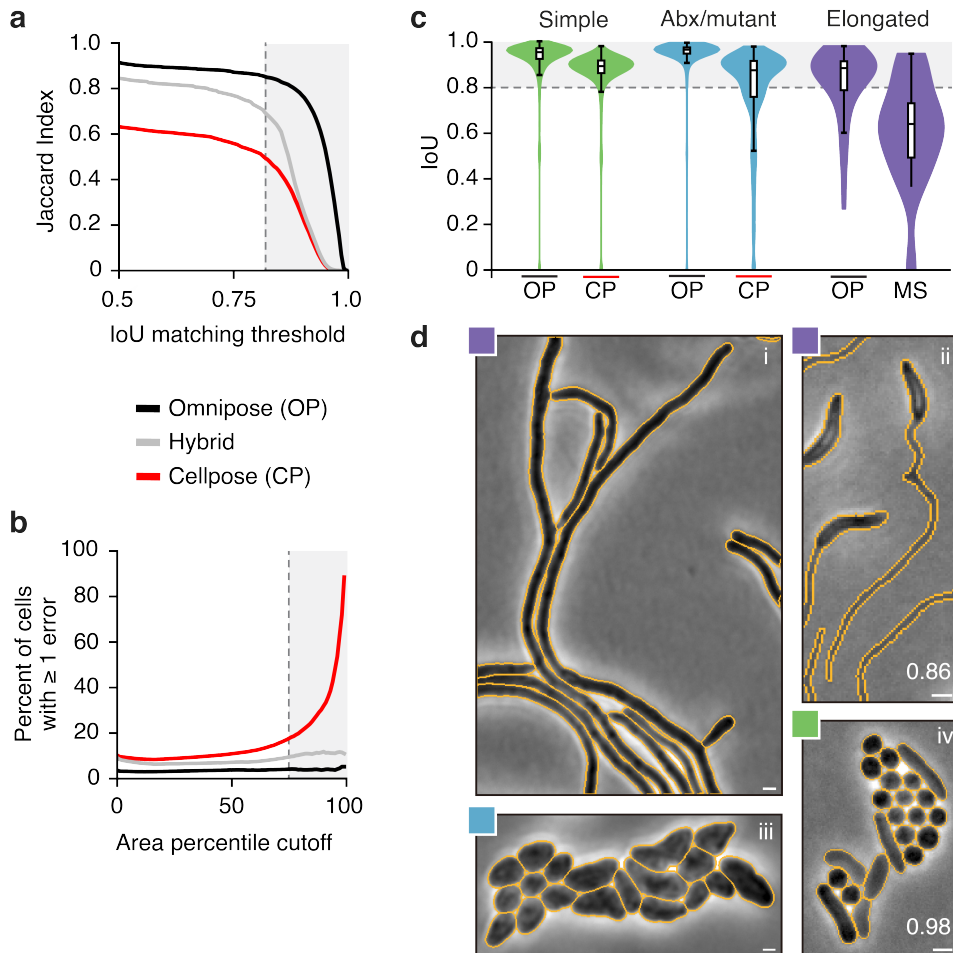
Fig. 4 | Omnipose outperforms Cellpose. (**a**) Overall performance measured by Jaccard Index (JI). The hybrid method (gray) is a variant of Cellpose that uses the original center-seeking flow output and the mask reconstruction of Omnipose. Gray box represents IoU ≥ 0.8. (**b**) Quantification of segmentation performance by cell size. The percent of cells with at least one segmentation error is computed for cells in each area percentile group from 1 to 100. Gray box represents the top quartile. (**c**) Omnipose IoU distribution on our dataset compared to the next highest performing algorithm in each of three cell categories. (**d**) Example micrographs and Omnipose segmentation. Mean matched IoU values shown. Bacteria displayed are (*i*) *Streptomyces pristinaespiralis,* (*ii*) *Caulobacter crescentus* grown in HIGG media, (*iii*) *Shigella flexneri* treated with A22, (*iv*) mix *of Pseudomonas aeruginosa, Staphylococcus aureus, Vibrio cholerae*, and *Bacillus subtilis*. Scale bars are 1 μm.
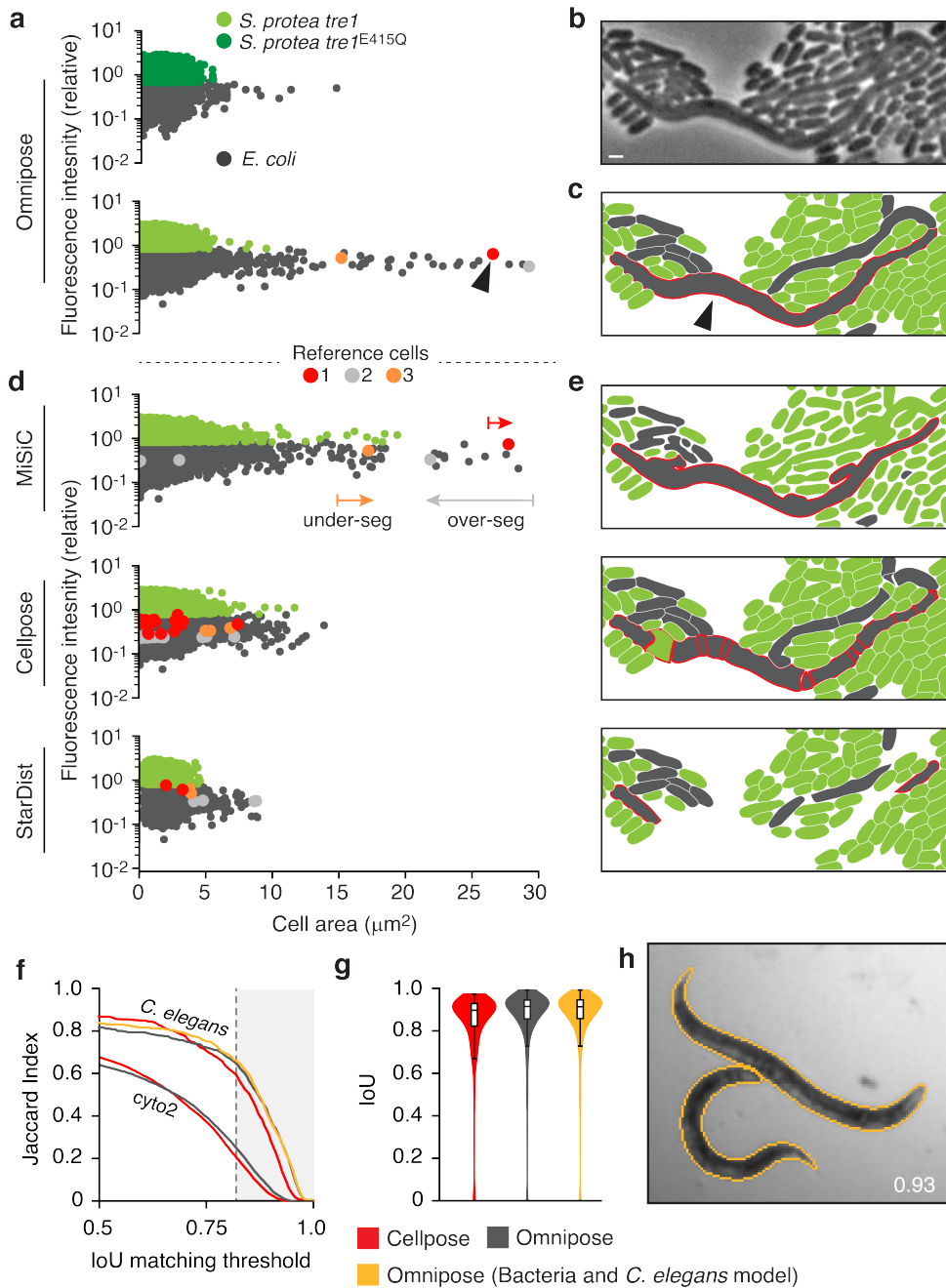
**Fig. 5 | Omnipose can be applied to the study of bacterial and non-bacterial systems.** (**a**) Fluorescence/area population profile according to Omnipose segmentation in control and experimental conditions. K-means clustering on GFP fluorescence distinguishes *S. proteamaculans tre1/tre1^{E415Q}* (light/dark green markers) from *E. coli* (gray markers). (**b**) Example of extreme filamentation of *E. coli* in response to active Tre1. (**c**) Omnipose accurately segments all cells in the image. Largest cell indicated with black arrow. (**d**) MiSiC predicts large cell masks over both species. Cellpose and StarDist fail to predict any cells above 15μm². (**e**) Example segmentation results highlighting typical errors encountered with MiSiC (under-segmentation), Cellpose (over-segmentation), and StarDist (incomplete masks). Mask mergers cause some *E. coli* to be misclassified as *S. proteamaculans*. Scale bar is 1 μm. (**f**) Performance of Omnipose and Cellpose on cyto2 and *C. elegans* datasets. Results for Omnipose trained on *C. elegans* (grey) or *C. elegans* and bacterial data (yellow) are shown. (**g**) IoU distribution for the masks predicted by each method on our *C.elegans* dataset. (**h**) Example segmentation of *C. elegans* in the BBBC010 dataset.

42
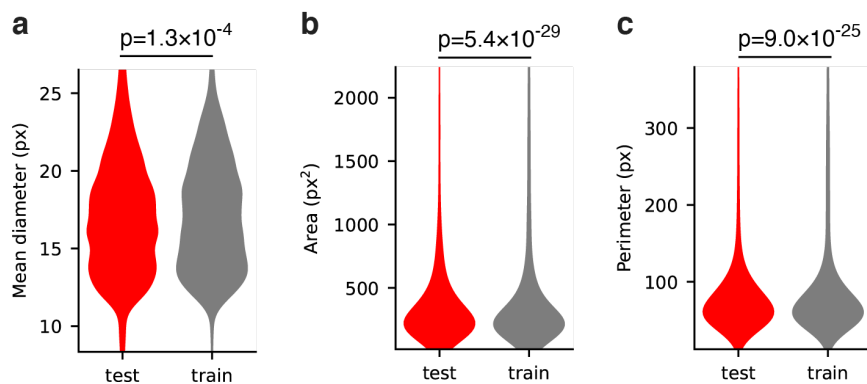
Extended Data Fig. 1 | Test dataset is representative of the training dataset. (**a**) Mean diameter, defined in Methods. (**b**) Cell area. (**c**) Cell perimeter. P-values are displayed for the two-sided KS test.
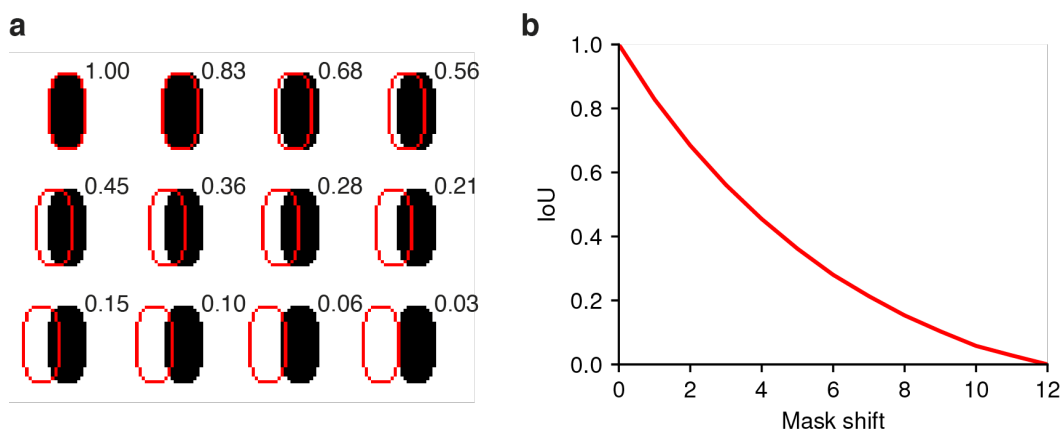
Extended Data Fig. 2 | IoU values for synthetic cell of typical size/resolution. (**a**) 0-12 pixel displacement of cell mask (red outline) and corresponding IoU values. (**b**) IoU decreases non-linearly for curved regions such as this synthetic cell.

44
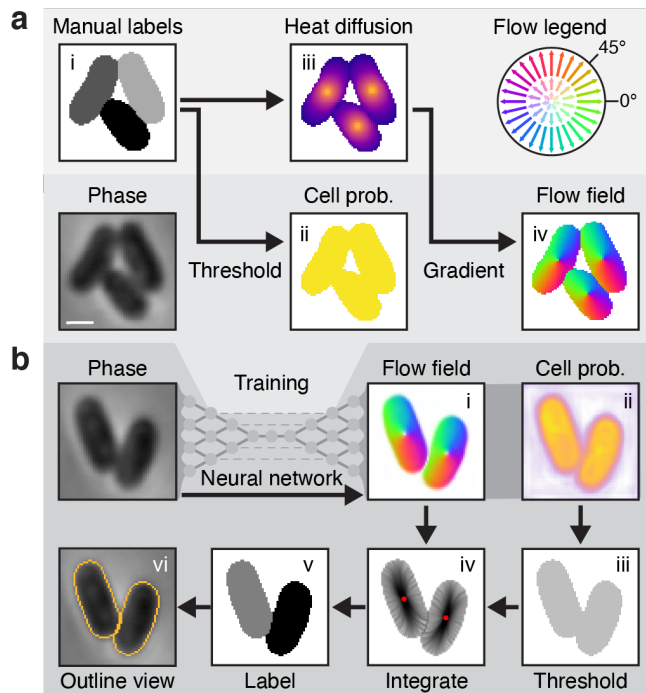
Extended Data Fig. 3 | Details of the Cellpose algorithm. (a) Stages of the Cellpose training pipeline. Ground truth masks (*i*) are converted to cell probability (*ii*) by binary thresholding and a heat distribution (*iii*) by simulated diffusion from the median pixel coordinate. The flow field (*iv*) is defined by the normalized gradient of (*iii*). Color-magnitude representations of this vector field follow the flow legend diagram. The phase, cell probability, and flow fields are used to train the network. **(b)** Stages of the cellpose prediction pipeline. Phase images are processed by the trained cellpose network into the intermediate flow field and cell probability outputs (*i-ii*). A binary threshold is applied to the probability to identify cell pixels (*iii*). Pixels are Euler-integrated under the flow field until they converge at common points. Boundary pixel trajectories are depicted in *iv*. Each pixel is assigned a unique label corresponding to the center to which it converged (*v*). This segmentation result is commonly depicted in an outline view (*vi*). Bacteria shown are *Escherichia coli*. Scale bar is 1 μm.
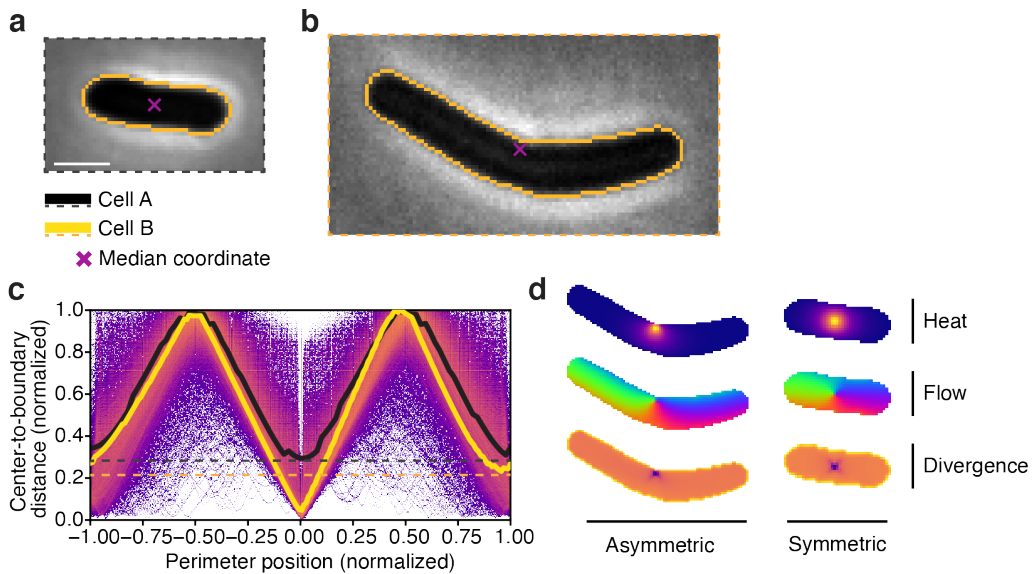
Extended Data Fig. 4 | Median coordinates are asymmetrically localized. (**a**) Center-to-boundary distance highlighted for two cells with non-projected median coordinates. Dashed lines indicate the larger of the two minima along the medial axis. (**b**) Rod-shaped *E.coli* with symmetric median coordinate. Symmetry of the center is reflected in A by equal high and low points corresponding to the extremal points along the long and short axes of the cell. (**c**) Curved *B. subtilis* with median coordinate asymmetrically close to the cell boundary. This asymmetry is reflected in A by a secondary minimum above the global minimum corresponding to the diametrically opposing point along the short axis of the cell. (**d**) These centers result in distinct flow fields reflecting the (a)symmetric of the cell center. Bacteria shown are (a) *Escherichia coli* and (b) *Bacillus subtilis*. Scale bar is 1 μm. Images scaled equivalently.
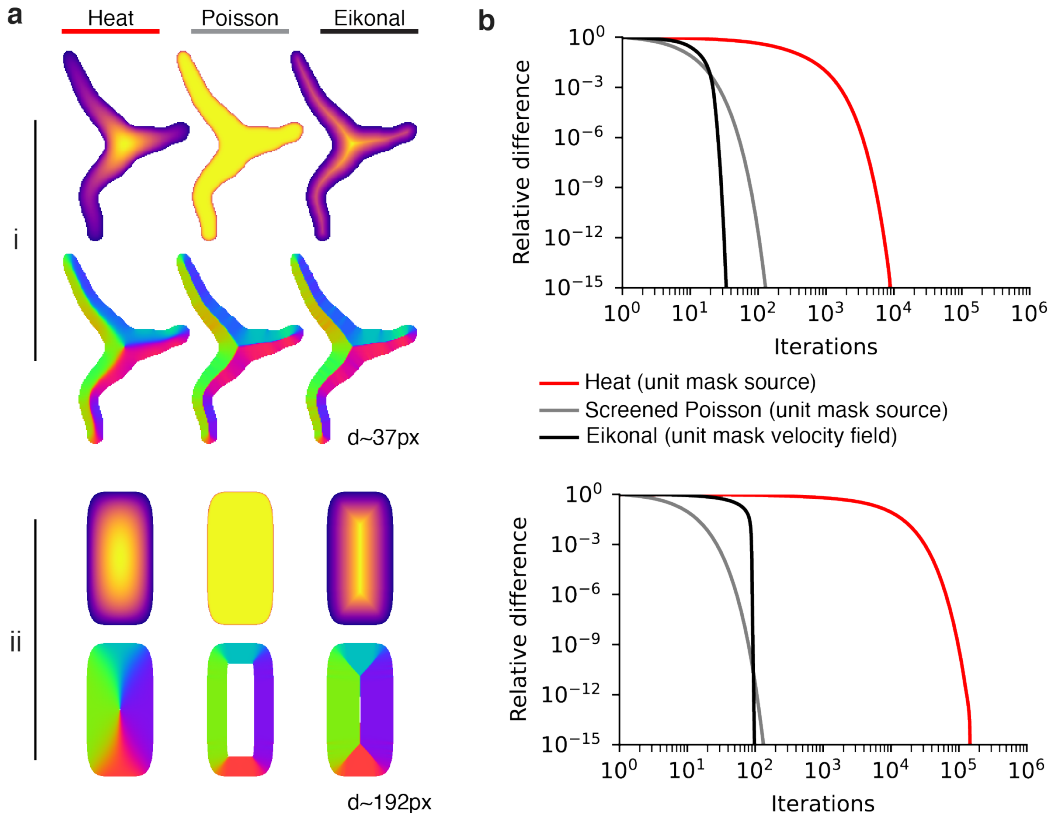
Extended Data Fig. 5 | Comparison of three algorithms for computing center-independent flow fields. Each field is defined by a partial differential equation with the mask at the source: time-independent heat equation, the screened Poisson equation, and the Eikonal equation. We solve these equations with iterative relaxation (see Methods). (**a**) Two example cells, the first drawn from our dataset with a mean diameter of 37px and a synthetic rod-shaped cell with a mean diameter of 192px. Cell (*i*) exhibits heat-derived flow components pointing toward the skeleton near boundaries and toward the global cell center at the skeleton. Center-seeking flow components become problematic for mask reconstruction for more complicated cell geometries, namely those with oscillating thickness. The screened Poisson and Eikonal equations produce nearly identical flow fields (same direction, normalized magnitude). Cell (*ii*) reveals a core flaw in the screened Poisson solution: its derivative exceeds our available numerical precision, leading to a vanishing flow field at the center where the solution plateaus. Any cells of this size or larger will exhibit this issue. (**b**) Convergence measured by the average difference at each iteration (maximum normalized to 1) for cells (*i,ii*). Our Eikonal solution converges faster than the other methods by a wide margin at typical cell diameters (*i*).
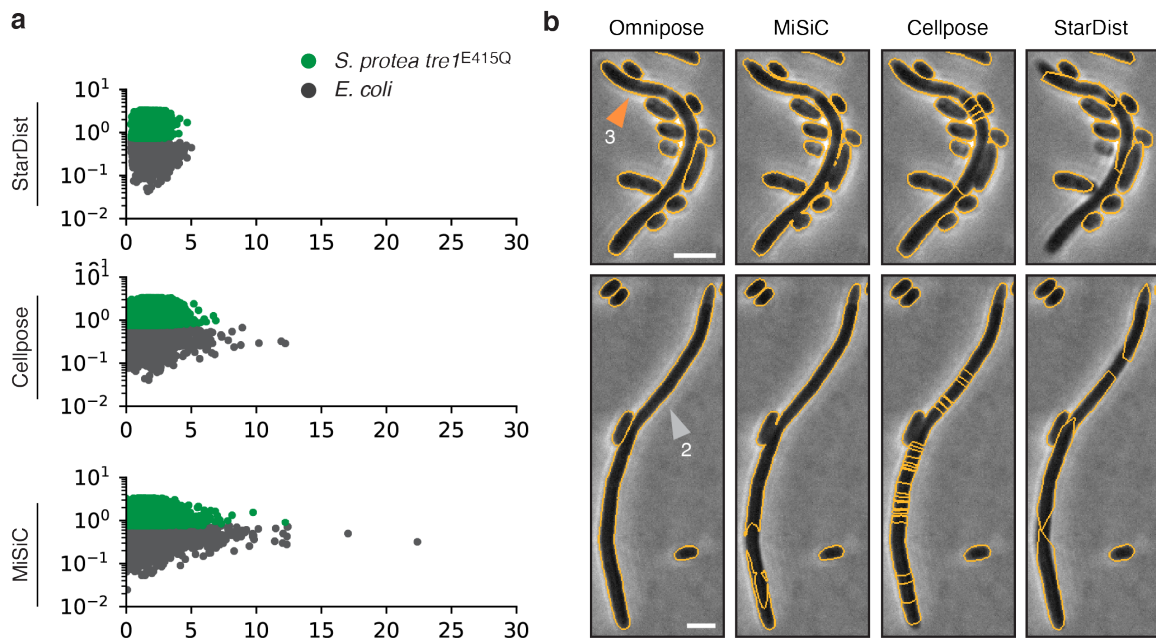
Extended Data Fig. 6 | Controls and additional examples. (a) Controls segmented by StarDist, Cellpose, and MiSiC. Notably, Cellpose and MiSiC exhibit an enrichment of larger cells even in the control, a consequence of both under-segmented (merged) cells as well as fragments of over-segmented large cells. **(b)** Cells 2 and 3 highlighted in orange and gray plotted in Fig. 5a,d. Scale bars are 1 μm.
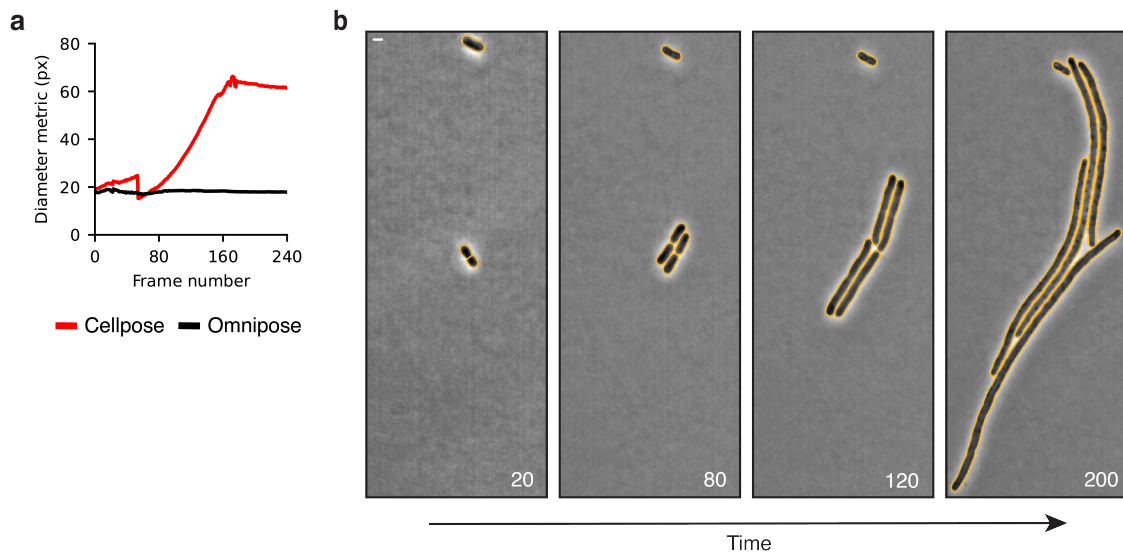
Extended Data Fig. 7 | Comparison of diameter metrics on a filamentous microcolony time lapse. (a). Cellpose diameter metric is the diameter of the circle with equivalent area. Omnipose diameter metric is proportional to the mean of the distance transform. (**b**) Bacteria displayed are *A. baylyi* transformed with a Δ*ftsN::kan* PCR fragment. Scale bar is 1 μm.

Extended Data Table 1.

Species	Strain	Image count	Cell Count	Cells in GT	Percent of GT	Notes
Escherichia coli	DH5α	1378	98200	9733	20.6	Dense microcolonies grown on minimal media. Thin phenotype. ITPG-induced GFP cytosol marker. Time lapse. Imaged by the Wiggins lab.
		141	4536	4395	9.3	Dense microcolonies on LB. Time lapse. Imaged by the Wiggins lab.
		2	2277	-	-	Treatment with cephalexin. Tn7::GFP. Imaged by the Mougous lab.
	CS703-1[62]	80	23169	1299	2.6	Mutant grown on LB and aztreonam. Elongated and branching phenotypes. Time lapse. Imaged by the Mougous lab.
Shigella flexneri	M90T	117	256618	1409	3.0	Treatment with A22. Tn7::GFP. Frames selected from time lapse after 1hr growth. Imaged by the Mougous lab.
		6	4482	4318	9.2	Treatment with cephalexin. Tn7::GFP. Frames selected from time lapse after 1hr growth. Imaged by the Mougous lab.
Francisella tularensis subsp. novicida	U112	5	20166	496	1.1	Small and extremely low-contrast cells. Tn7::GFP. Imaged by the Mougous lab.
Acinetobacter baylyi	ADP1[63]	2169	60601	3336	7.1	Deletion of essential gene *murA*. Rounded phenotype. Time lapse. Imaged by the Wiggins lab.
		241	1313	1133	2.4	Deletion of essential gene *ftsN*. Filamentous phenotype. Time lapse. Imaged by the Wiggins lab.
		540	10013	2227	4.7	Deletion of essential gene *dnaA*. Filamentous phenotype. Time lapse. Imaged by the Wiggins lab.
Burkholderia thailandensis	E264[64]	30	62005	5122	10.9	Selected panels from a self-intoxication experiment. Cells exhibit internal structure and low contrast in microcolonies. Tn7::GFP. Time lapse. Imaged by the Mougous lab.
Helicobacter pylori	LHS100[50]	15	13014	-	-	Helical phenotype. Grown, fixed, and stained with Alexaflour 488 in the lab of

Species	Strain					Description
						Nina Salama. Imaged by the Mougous lab.
		19	1668	701	1.5	Treated with aztreonam. Filamentous, helical phenotype. Grown, fixed, and stained with Alexaflour 488 in the lab of Nina Salama. Imaged by the Mougous lab.
Caulobacter crescentus	NA1000[52]	4	1787	756	1.6	Grown in HIGG media to induce stalk phenotype. Cultivation and imaging done in the lab of Yves Brun.
Streptomyces pristinaespiralis	NRRL 2958	17	2339	270	0.6	Grown on rich media to induce filamentous phenotype. Imaged by the Mougous lab.
Vibrio cholerae	A1552[65]	2	2627	2265	4.8	Cells have short but curved morphology and form dense, low-contrast microcolonies. Tn7::GFP. Obtained from the lab of Fitnat Yildiz. Imaged in the Mougous lab.
Serratia proteamaculans *E. coli*	568 DH5α	43	100146	1244	2.6	1:1 mixture. *S.p.* labelled via Tn7::GFP, *E.c.* unlabeled. Time lapse. Imaged in the Mougous lab.
Pseudomonas aeruginosa *Staphylococcus aureus*	PAO1[66] USA300	3	2662	3688	7.8	1:1 mixture. *P.a.* labelled via Tn7::GFP, *S.a.* unlabeled. Imaged in the Mougous lab.
P. aeruginosa *S. aureus* *V. cholerae* *Bacillus subtilis*	PAO1 USA300 A1552 HM1350	21	33281	4678	9.9	1:1:1:1 mixture. *P.a.* and *V.c.* labelled via Tn7::GFP, *S.a.* and *B.s.* labelled with red membrane dye. Imaged in the Mougous lab.
		4833	700904	47070	100	